ICING EFFECTS ON A HORIZONTAL AXIS WIND TURBINE

JIEQUN RONG, B.Eng.

ICING EFFECTS
ON
A HORIZONTAL AXIS WIND TURBINE

BY

©RONG, JIEQUN, B.Eng.

A thesis submitted to the School of Graduate
Studies in partial fulfillment of the degree of
Master of Engineering

Faculty of Engineering and Applied Science
Memorial University of Newfoundland
DECEMBER, 1991

St. John's Newfoundland

ISBN 0-315-73297-0

Abstract

Freezing precipitation has extremely high incidence in parts of Atlantic Canada and this condition is expected to severely reduce the energy output from aerogenerators. This project was aimed at the evaluation of effects of freezing precipitation conditions on the output of wind turbine generators. Major achievements have included the simulation of freezing rain events, in particular, glaze icing in a cold room and in field applications; testing of a NASA LS(1)-0417 wing section in the wind tunnel under simulated icing conditions; and theoretical evaluation of performance degradation by icing on blades for two horizontal axis wind turbines, that is, a 2.5 m diameter wind turbine and a Carter-23 wind turbine, by using lifting-line theory.

An experiment to model the form of ice accumulation on a horizontal axis rotor was done in a cold room. Ice profiles on the blade sections were recorded. Wind tunnel tests for an airfoil used typically for wind turbine blades were done with various simulated glaze and rime ice accretions attached to the leading edge of the airfoil. Lift and drag coefficient data were obtained for angles of attack from $-6°$ to $90°$. A theoretical method was used for estimation of degradation of aerodynamic performance of horizontal axis wind turbines in icing conditions. The theory used was based on marine-propeller lifting line theory that had been adapted for wind turbine use. This made use of airfoil section data obtained from wind tunnel tests. A simulated icing test on a full scale horizontal axis wind turbine was performed at the Atlantic Wind Test Site.

The cold room icing test gave a better understanding of the blunt shaped glaze ice accretion on the leading edge of blade sections where the wind speed was relatively high. The theoretical estimations showed that icing events, associated with

ambient temperatures close to freezing point and high liquid water content in the air, could destroy the performance of wind turbines completely. The wind turbine field test showed that a progressive power reduction occurred during a simulated freezing event and a complete loss of power from the wind turbine generator was encountered after a short time period of freezing precipitation. The wind tunnel tests for the airfoil with simulated ice accretions on the leading edge revealed that increase of drag coefficient and decrease of lift coefficient on the iced blade sections of a wind turbine were the main reasons that caused the power output from a wind turbine to drop.

Acknowledgements

I thank the following organisations for providing financial support: Energy, Mines and Resources, Canada; the Natural Sciences and Engineering Research Council of Canada; Department of Mines & Energy, Government of Newfoundland and Labrador; Memorial University of Newfoundland; and the Atlantic Wind Test Site. I also thank the technicians in the Thermal laboratory, Fluids Laboratory and machine shop, as well as all the members of the Center for Computer Aided Engineering of our faculty, for their generous help. Thanks are also due to Mr. C. Brothers, Mr. M. Lodge and all the technicians in the Atlantic Wind Test Site for their instructive advice during the wind turbine field test. Finally, the author is indebted to Dr. N. Bose, who has acted as supervisor and provided patient advice and guidance throughout this study.

Contents

List of Figures

List of Tables

Chapter 1

Introduction

As a form of renewable energy, wind energy offers many environmental, economic and social benefits. The modern windpower industry was born in the chaos of the world energy crisis of the 1970's, though wind has been generating power for centuries. Among the developed countries, the United States of America is in the leading position in utilization of wind energy; wind generates close to 2 TeraWatt hours per year in California, which is 85% of generated wind power in the world. European countries, where wind power technology originated, have made tremendous progress in developing new wind energy technology in recent years. Canada, which is well known for its rich natural resources, is aware of the importance of exploring such kinds of renewable energy technology in order to conserve natural energy resources.

The world energy crises and global warming impact the whole world. More and more countries have been making wind energy into utility-grade power by improving the efficiency of wind conversion systems and reducing wind energy generation cost per kilowatt-hour. Increasing applications of wind turbines occur not only in regions where the wind resource is plenty, but also in cold regions where icing events during winter are prevalent. The working properties of wind turbines can

be altered substantially under atmospheric icing conditions [1,2,3]. This has been emphasized by the present research [4,5,6,7].

Freezing rain, which is one of the main types of icing event in parts of Canada, can reduce total energy output from a wind turbine and therefore increase the cost of utility power generation due to ice accretion on the rotors. Rotor icing can result in serious degradation of aerodynamic performance of a wind turbine by altering the geometry of blade sections and thus, changing the properties of flow field around each blade section. From statistics for the period of 1967-76 [8], it has been shown that parts of Atlantic, Arctic, sub-Arctic and Coastal regions of Canada have a high incidence of freezing rain and freezing drizzle events during winter, and these conditions result in potential annual energy losses from wind conversion systems that are operating in cold regions [8].

Typically, there exist two classes of ice accretion on wind turbine blades [1,2]; these are known as glaze and rime ice, as shown in figures 1.1 and 1.2. The icing formation on a rotor is governed by the temperature of the water droplets, their size, the liquid water content (LWC) of the air, as well as the rate at which they strike a surface. Rime ice results from a lower air and droplet temperature and low liquid water content in the air. Highly supercooled water droplets freeze immediately on impinging on a blade leading to higher porosity deposits and hence lower density of the ice. They form a soft milky covering of streamlined shape [1,2]. Glaze ice forms at temperatures just below freezing point in air with a high liquid water content, larger diameter of the water droplets as well as high relative impact speed. Under glaze icing conditions, droplets do not freeze immediately on impingement, due to lower supercooling, but run first along the surface some distance [1,2], as illustrated in figure 1.3. In the case of glaze icing or wet icing, the aerodynamic pressure plays

an important role in forming the ice profile around the leading edge of a blade. Near the stagnation point, the droplets are forced to move along the surface of the blade away from the stagnation point or line, due to the high pressure gradient near the leading edge. The result is a deposit of higher density transparent ice with two protrusions which are considered to degrade overall performance of a wind turbine much more significantly than rime ice deposits.

A series of experimental and theoretical studies were done to show the severity of blade icing on horizontal axis wind turbines. Based on a lifting-line theory [9,10,11], a numerical method was adapted to predict the degradation of aerodynamic performance for horizontal axis wind turbines due to ice accretion. This theory was developed for marine screw propellers and was adapted for wind turbine use by Small and Bose [12,13] and Bose [14], and further modified for wind turbines with an iced rotor. The performance calculation was done by using lifting-line theory together with experimental data of lift and drag coefficients for the blade section over a wide range of angles of attack. These data were provided by wind tunnel tests for wing sections with several simulated ice shapes formed under glaze and rime icing done under this study and also documented by Wilder [15] and Bragg [16]. The computational results showed that typical glaze icing conditions completely destroyed the aerodynamic performance of a Carter-23 wind turbine and a small wind turbine with 2.5 m diameter rotor over tip speed ratios from 0.5 to 12. The results also showed that rime ice had less effect on the overall performance when compared with glaze ice; power reduction by rime icing was 30% for the Carter-23 wind turbine and 49% for the 2.5 m diameter wind turbine.

Wind turbine model icing tests were done under typical freezing rain conditions which were simulated inside a cold room at Memorial University of Newfoundland.

The ice profiles around the rotor blades were documented for later wind tunnel tests. Full scale wind turbine icing field tests were conducted at the Atlantic Wind Test Site in Prince Edward Island, Canada. Full scale wind turbine test results showed that freezing precipitation on the rotor reduced the output of the wind turbine by 100% shortly after the freezing event and could make the whole system go out of balance due to the extra loads exerted on the rotor by ice accretion.

Although icing is a critical problem for a wind conversion system operating in the cold regions during winter, insufficient attention has been paid to it in the past. The purpose of this project was to let experts and planners, who are involved in the utilization of renewable energy, be aware of the severity of the wind turbine icing problem and also to obtain a methodology to predict precisely and completely the performance degradation of horizontal axis wind turbines from icing. Recommendations were also made for possible later studies of wind turbine de-icing technology.

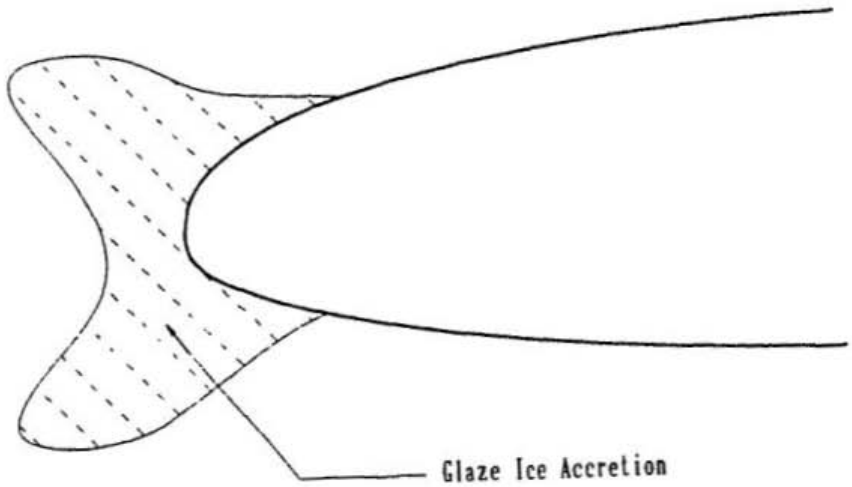

Figure 1.1: Glaze ice formation.

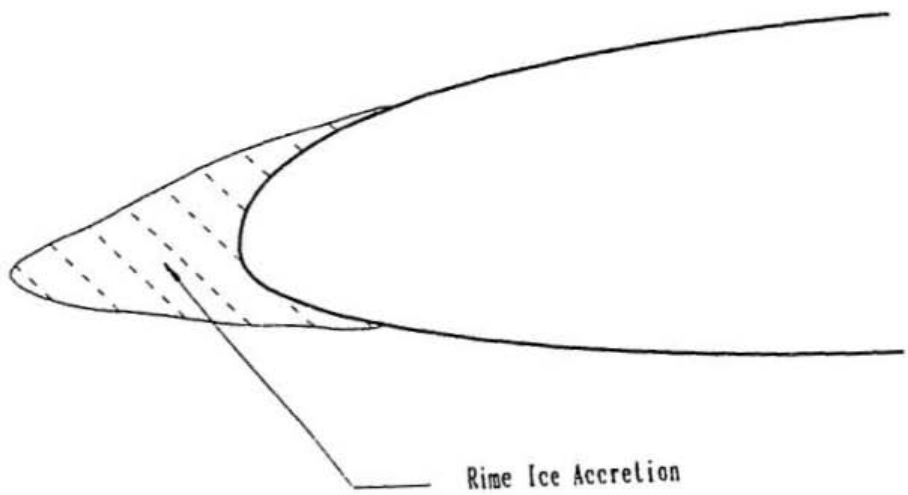

Figure 1.2: Rime ice formation.

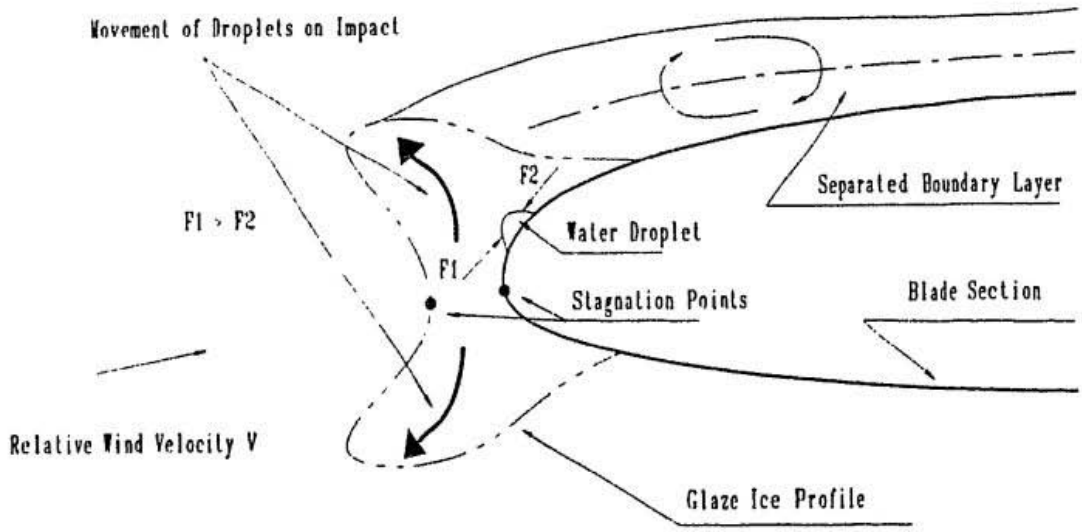

Figure 1.3: Mechanism of glaze ice formation.

Chapter 2

Ice Accretion Process on a Rotor

When water droplets impinge on the surface of blades, they begin to spread, are nucleated and then begin to freeze. During that process, they may coalesce with other droplets which are only partially frozen; splashing also occurs if the droplets are sufficiently large [17].

2.1 Types of Atmospheric Icing

Icing from atmospheric sources can result from contact with supercooled clouds or fog droplets, from freezing precipitation or wet snow. Each of these types of icing is associated with particular meteorological conditions and can result in typical types and accumulations of ice on a wind turbine rotor.

Freezing precipitation results when liquid precipitation falling from warm air aloft is cooled below the freezing point as it falls through a layer of cold air nearer the earth's surface; this can be in the form of freezing rain or freezing drizzle. Freezing rain is defined as having drops of more than 0.5 mm in diameter and rates that range from less than 2.5 mm per hour to greater than 7.6 mm per hour. Freezing drizzle is usually defined as fairly uniform precipitation composed exclusively of fine drops of water of diameter less than 0.5 mm. The rate of drizzle

falling range from less than 0.3 mm per hour to greater than 0.8 mm per hour [18]. Thus accumulations of ice from freezing rain would be greater than from freezing drizzle. Both events are usually associated with glaze ice accretion.

Cloud and fog droplets can exist in a liquid state at temperatures well below freezing point. When these droplets come into contact with an object, they freeze on impact, forming rime ice. Due to the lower liquid water content of the air, this type of icing generally does not pose a problem for a wind turbine except when it occurs in association with high winds in which large amounts of water are brought into contact with the object, ice build up is then considerable.

Wet snow, that is blown against an object, may stick and change to ice with lower density than that formed from freezing rain [18]. These different atmospheric icing conditions change the behaviour of the wind turbine in different ways. The icing effects on wind turbines mainly associated with freezing rain events will be discussed in the following chapters. This type of icing event causes glaze ice accretion on a wind turbine's rotor.

2.2 Nucleation of Water Droplets

The formation of an ice crystal from a water droplet within a homogeneous fluid demands the expenditure of a certain quantity of energy in creation of a solid surface. Therefore, the total quantity of work required to form a stable crystal nucleus is equal to the work required to form the surface and the bulk of the particle, which is usually called free energy. According to Michel [19], the free energy ΔG_c in the homogeneous fluid required to form a spherical particle is given

by

$$\Delta G_c = \frac{16\pi e_{cl}^3 \theta_o^{*2}}{3L^2 \Delta\theta^2} \tag{2.1}$$

and the rate of nucleation of water droplets is

$$J = A exp[\frac{-16\pi e_{cl}^3 \theta_o^*}{3kL^2 \Delta\theta^2}] \tag{2.2}$$

where e_{cl} is the surface energy of the crystal in contact with the liquid in mJ/m^2; θ_o^* is the solid-liquid equilibrium temperature in Kelvin; $\Delta\theta$ is the supercooling of the liquid in Kelvin; L is the latent heat in kJ/kg; k is the Boltzmann gas constant; and A is a constant. In reality, the fluid is heterogeneous. For the same critical free energy required for nucleation and for a similar crystal form, the amount of supercooling for homogeneous nucleation, $\Delta\theta_o$, will then be reduced [19] and the value of supercooling for heterogeneous fluid $\Delta\theta_n$ becomes

$$\Delta\theta_n = \Delta\theta_o \sqrt{\frac{1 - cos\gamma}{2}}, \tag{2.3}$$

where γ is usually taken as the angle of contact between the ice and the nucleating material. At the limit, when the nucleation is initiated with an ice crystal, $\gamma = 0$ and then the supercooling required for nucleation, $\Delta\theta_n = 0$. This is expected because no supercooling is required to grow ice from any existing ice nucleus. It is usually considered that usual inorganic nucleation in static conditions has a temperature threshold of about $-3.5°C$ while, for ordinary tap water an average nucleating temperature is found to be $-2.5°C$ [19]. From equation 2.2, the rate of water droplet nucleation increases with the increase of degree of a water droplet's supercooling, $\Delta\theta$, and therefore, determines the icing process on wind turbine blades that will be discussed in the next sections.

2.3 Water Droplet Impingement

When water droplets are moving toward the blades, their momentum affects the way in which they impinge on the blades; the bigger the droplets the higher the possibility that the droplet will impinge on the blade surface. The behaviour of the water droplets on impingement at the leading edge of the blade can be considered to be similar to movement towards an object with a cylindrical front edge with local radius, r. The rate of the water droplet's capture varies along the surface of the blade at different locations. A detailed mathematical description was presented by Lozowski [20]. The analysis begins by considering each droplet category, its Reynolds number, Re, and its Langmuir inertia parameter, K,

$$Re = \frac{DU\rho_a}{\mu_a}, \tag{2.4}$$

$$K = \frac{\rho_w U D^2}{9\mu_a D_c}, \tag{2.5}$$

where ρ_a and ρ_w are the density of the air and water, μ_a is the viscosity of the airstream D_c is the diameter of cylinder, D is the diameter of water droplet and U is the freestream velocity, and a modified inertia parameter,

$$K_0 = 0.125 + \frac{K - 0.125}{1 + 0.0967 Re^{0.6367}}. \tag{2.6}$$

With the use of K_0, values of the stagnation line collision efficiency, the total collection efficiency, E, on the profile and the maximum impingement angle, θ_m, along the cylindrical surface can be derived [20].

Figure 2.1 shows the relationship between the total collection efficiency E and the Langmuir inertia parameter K for a cylindrical surface with radius R_c documented from Mortimer [1], where Φ is a Langmuir and Blodgett impingement

parameter defined as

$$\Phi = \frac{18\rho_a^2 V R_c}{\mu_a \rho_w}. \tag{2.7}$$

The collection efficiency, E, in figure 2.1, is governed greatly by the droplet size, the radius of the cylinder or the leading edge of the blade. The bigger the water droplets and the smaller the radius of the leading edge, the more water droplets impinge or are captured on the blade. This is due to increasing Langmuir inertia parameter, K, and reducing Langmuir and Blodgett impingement parameter, Φ. Resultant wind speed, V, can affect the collection efficiency, E, in a negative way by increasing, Φ.

2.4 Critical Liquid Water Content

If water is to freeze, the latent heat of fusion must be released and has to be removed. In most situations the rate of freezing is limited by the rate at which the heat can be dissipated to the environment. The steady-state heat balance equation that is assumed to describe the thermodynamics of accretion may be written as [21]

$$q_c + q_e + q_v + q_K + q_f + q_w + q_i + q_r + q_w^* + q_f^* = 0 \tag{2.8}$$

where

q_c is the convective heat loss between the accretion and the airstream by conduction and convection;

q_e is the evaporative heat flux;

q_v is the heat flux due to aerodynamic heating;

q_K is the heat flux due to the conversion of droplet kinetic energy into heat;

q_f is the latent heat flux to the accretion due to freezing of some, or all, of the directly impinging water;

q_w is the heat flux between the directly impinging water and the underlying accretion;

q_i is the heat flux between the accretion and the underlying surface;

q_r is the radiative heat flux between the accretion and the airstream;

q_w^* and q_f^* are similar to q_w and q_f but are for unfrozen water.

All of the heat fluxes q are assumed to be positive if they add heat to the accretion, and negative in the opposite case. The terms of radiation and internal conduction, q_r and q_i are usually small and can be ignored compared with other terms. The heat flux or heat convection q_c is given by

$$q_c = h(t_a - t_s), \tag{2.9}$$

where t_a and t_s are respectively the freestream air temperature and the steady-state accretion surface temperature. The quantity h is the heat transfer coefficient and can be written in terms of the Nusselt number N_u,

$$h = \frac{k_a N_u}{D_c}, \tag{2.10}$$

where k_a is the thermal conductivity of the airstream. The value of the Nusselt number, N_u, can be found by considering the specific geometry of the body [20] and may be written approximately, for a smooth surface, as

$$N_u(\theta) = Re^{0.5}[1 - (\frac{2\theta}{\pi})^3] \tag{2.11}$$

and for a rough cylinder as

$$N_u(\theta) = Re^{0.5}\{2.4 + 1.2sin[3.6(\theta - 0.440)]\}. \tag{2.12}$$

In addition to the heat convection, there is a transfer of latent heat due to the evaporation or sublimation of water vapour from the surface. According to Reynolds'

analogy [20], this term can by written as

$$q_e = h(\frac{P_r}{S_c})^{0.63}\frac{\epsilon l_v}{pc_p}(e_a - e_s), \tag{2.13}$$

where P_r and S_c are the Prandtl and Schmidt number; ϵ is the ratio of the molecular weight of water vapour to dry air; p is the static pressure in the free stream; c_p is the specific heat capacity at constant pressure for dry air; e_a and e_s are the saturation vapour pressure of moist air at t_a and t_s; and l_v is the latent heat of evaporation. If the accretion is dry, that is, $t_a < 0°C$, the latent heat of sublimation might be more appropriate, although even in this case, a film of water may exist on the accretion surface for the finite time required for the impinging water to freeze completely. The aerodynamic heating term is given by

$$q_v = \frac{hr_cU^2}{2c_p} \tag{2.14}$$

where r_c is the local recovery factor on the cylinder given by

$$r_c = 0.75 + 0.25cos2\theta. \tag{2.15}$$

This latter expression is based on the work of Seban [22] and takes into account the adiabatic heating arising from compression of the air which is decelerated in passing around the cylinder, as well as frictional heating within the boundary layer, which should be considered when rotational speed of wind turbine's rotor and the air speed are high. The kinetic energy flux of the droplets q_k is given approximately by

$$q_k = \frac{1}{2}R_wU^2. \tag{2.16}$$

where R_w is droplet mass flux. The droplets are impinging at the freestream air speed, and all of their kinetic energy is converted to heat. The latent heat flux due

to the impinging water is

$$q_f = R_w l_{fs} \tag{2.17}$$

where l_{fs} is the latent heat of freezing at the temperature of t_s. The heat flux between the accretion and impinging droplets is that required to warm the droplet from the free airstream temperature, t_a, to the steady state surface temperature of the deposit, t_s, that is,

$$q_w = R_w c_w (t_a - t_s), \tag{2.18}$$

where c_w is the average specific heat of water between the temperatures of t_a and t_s. The same algorithm can be applied to q_w^* and q_f^* for unfrozen or run back water in which R_w is the run back water mass flux and t_a is the incoming temperature of the run back water.

The critical value of the liquid water content LWC_c in the air, below which all water droplets freeze on impingement, can be obtained by considering the heat balance in equation 2.8 and setting the surface temperature, t_s, just at the melting point,

$$LWC_c = -h \frac{(t_a - t_s) + (\frac{Pr}{Sc})^{0.63} (\frac{\epsilon l_v}{pc_p})(e_a - e_s) + \frac{rU^2}{2c_p}}{EU(\frac{2}{\pi})[c_w(t_a - t_s) + l_f + \frac{U^2}{2}]} \tag{2.19}$$

in which components of run back water are neglected. As the deposit temperature cannot exceed 0°C, there is, for given ambient temperature, air speed and droplet size, a critical liquid water content LWC_c at which all of the accreted droplets may be just frozen. If the LWC is lower than the critical value all of the droplets freeze and the deposit temperature is below 0°C. This is usually associated with rime ice growth or dry growth. If the liquid water content is above the critical value, the result of heat balance between the air and surface of ice accretion is that the temperature of the ice accretion is equal to the melting point and there maybe

a portion of unfrozen water on the surface of the accretion moving around blade surface. This extra portion of water will be driven by the external forces, such as the aerodynamic force around blade section, and causes a formation of glaze ice with blunt shapes on the blade surface. One can also assume that the liquid water content is kept at a certain value and let the ambient temperature change. There should be a critical ambient temperature t_c existing at which the water droplets impinging on the blades are just frozen. Also some special icing events occur, in which glaze ice still exists at lower ambient temperature due to very high liquid water content in the air.

Experimental results show that higher liquid water content in the air and higher ambient temperature will cause the original blade section profile to be distorted considerably due to the large portion of unfrozen water running on the surface of the ice accretion. Figure 1.3 shows the mechanism of glaze ice formation.

2.5 Rate of Ice Accretion

The rate of ice accretion on the blades depends mainly on the atmospheric conditions: the liquid water content in the air; ambient temperature; droplet's size; relative air speed to the blade; and the geometric size of the blade. For a blade with radius, R, of the cylindrical leading edge, the rate of the ice accretion, R_g, was expressed by Mortimer [1], as

$$R_g = 3600V \times LWC \times E \tag{2.20}$$

and this is illustrated in figure 2.2.

The rate of accretion is strongly governed by the droplet's size and liquid water content in the air in positive ways. The higher the liquid water content the higher

the possibility for the blade to capture the water droplets. Also, droplets will deviate, due to their momentum, from the curvature of the streamlines in the vicinity of the leading edge: the larger the droplet size, the higher their momentum and the more droplets hit the blade. Higher sensitivity of icing growth rate occurs when water droplet size is small as shown in figure 2.2. Liquid water content in the air is also critical for icing rate; higher sensitivity to LWC occurs when droplet size is less than 20μm. The radius of the leading edge of the blade and the resultant relative wind velocity both affect the collection efficiency, E, in a negative way. Increasing wind speed causes an increase in rate of water droplet impingement on the blade and hence rate of accretion.

However, the rate of ice accretion referred to above is true only if it satisfies the icing nucleation conditions discussed in section 2.4. If the water droplets captured by the blades cannot freeze within a certain time, the aerodynamic force, centripetal force and even gravity force will cause the droplets to be shed off from the wind turbine rotor and therefore there will be no ice accretion on the wind turbine blades.

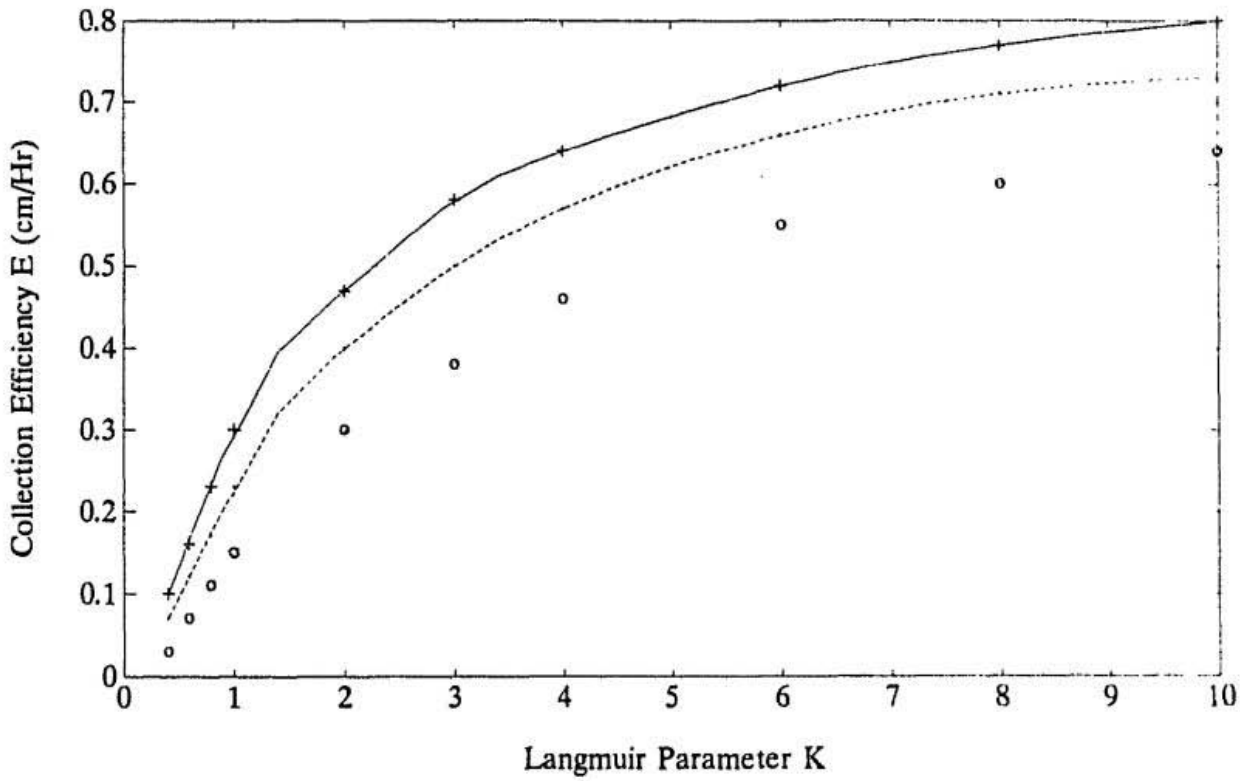

Upper curve: $\Phi = 100$
Middle curve: $\Phi = 1000$
Lower curve: $\Phi = 10000$

Figure 2.1: Collection efficiency of a cylinder.

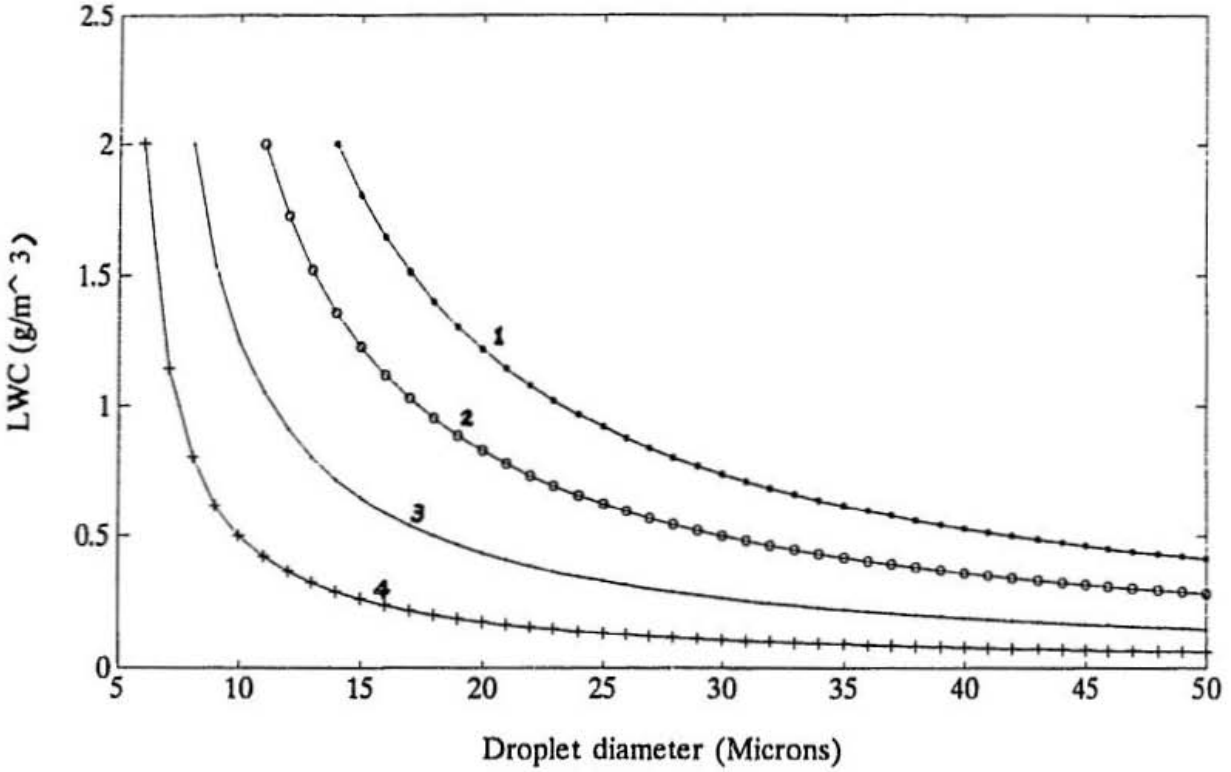

Curve 1: $R_g = 15 g/cm^2/hr$
Curve 2: $R_g = 10 g/cm^2/hr$
Curve 3: $R_g = 5 g/cm^2/hr$
Curve 4: $R_g = 1 g/cm^2/hr$
Rg: Rate of icing accretion

Figure 2.2: Rate of icing accretion.

Chapter 3

The Theory of Propeller Type Wind Turbines

Propeller type wind turbines can be considered to be airscrews which extract energy from the air and convert it into other forms of energy. This is in contrast to a propeller which expels energy into the air or water from another energy source. The similarity of the propeller and the wind turbine enables the same theoretical development to be followed for performance analysis.

Propeller theory developed along two independent methods of approach, one of which has been called momentum theory and the other, blade element theory. The basis of the theory is the determination of the forces acting on the rotor to produce the motion of the fluid. The approach of blade element theory is concerned with the forces produced by the blades as a result of the motion of the fluid. A more detailed model was developed for propellers and generalized for wind turbines by Glauert [23]. This utilized both the axial momentum and blade element theories and a series of relationships were developed to determine the performance of a wind turbine.

Modern propeller theory developed from the concept of free vortices being shed

from the rotating blades. These define a slipstream and generate induced velocities at the blades and in the wake. This can be attributed to the work of Joukowski [24], for induced velocity analysis; to Betz [25], for rotors with minimum energy loss; to Goldstein [9], for circulation distribution, particularly for effects of a finite number of blades and to Eckhardt and Morgan [26], for general improvement and application. This theory has been referred to by a number of names, notably: vortex theory, circulation theory and lifting-line theory.

3.1 Ideal Power Coefficient for Propeller Type Wind Turbines

To begin to understand the mechanism of rotor power absorption from winds, the Rankine-Froude actuator disc theory provides a start. As an initial approach, ideal conditions are considered for wind turbine operation. The function of a wind turbine is to extract energy from the air and to produce mechanical energy. As a first approximation, to determine the maximum possible output of a wind turbine from momentum theory, the following assumptions are made,

1. blades operate without frictional drag;
2. a slipstream separates the flow passing through the rotor disc from that outside the disc;
3. the static pressure inside and outside of the slipstream far ahead of and behind the rotor are equal to the undisturbed free-stream static pressure;
4. thrust loading is uniform over the rotor disc; and
5. no rotation is imparted to the flow by the disc.

Applying the momentum theorem to the control volume in figure 3.1, the thrust,

T, can be expressed as

$$T = \rho A U (V_1 - V_2) \tag{3.1}$$

where V_1 is the free stream velocity far ahead of the rotor, V_2 is the wake velocity and U is the velocity through the rotor disk. By applying Bernoulli's equation to the flow upstream and downstream of the wind turbine, and substituting into equation 3.1, one obtains

$$U = \frac{V_1 + V_2}{2}. \tag{3.2}$$

This result states that the velocity through the turbine is the average of the wind velocity ahead of the turbine and wake velocity behind the turbine. By defining the axial induction factor a as,

$$U = V_1(1 - a) \tag{3.3}$$

the wake velocity can be expressed as

$$V_2 = V_1(1 - 2a) \tag{3.4}$$

and the induced axial velocity u_a behind the rotor disc can be expressed as

$$u_a = 2aV_1. \tag{3.5}$$

From the expression for the kinetic energy which can be absorbed by the wind turbine, the ideal power output from wind turbine, P, becomes

$$P = 2\rho A V_1^3 a(1 - a)^2 \tag{3.6}$$

where A is the swept area of the wind turbine, and therefore the maximum power occurs when $dP/da = 0$ which is

$$P_{max} = \frac{8}{27}(\rho A V_1^3) \tag{3.7}$$

The power coefficient of the wind turbine, C_p, is defined as

$$C_p = \frac{P}{\frac{1}{2}\rho A V_1^3} \tag{3.8}$$

Using the value of P_{max}, the ideal power coefficient reaches approximately 0.593.

In reality, wake rotation exists due to blade rotation. The induced tangential velocity component in the wake u_t can be expressed as [12]

$$u_t = 2a'\Omega r \tag{3.9}$$

which is twice the value of the induced velocity at the rotor disk, where a' is an induced tangential factor and Ω is a rotational speed of the rotor. The resultant induced velocity at the rotor disk is perpendicular to the resultant relative wind velocity [10] as shown in the figure 3.2.

3.2 Lifting-line theory

The lifting-line theory used for the horizontal axis wind turbines analyzed here was adapted from screw propeller circulation theory and provides a link between a blade section operating in two dimensional flow and that operating as a part of a screw. The blade is replaced by a bound vortex line. This theory is based on the concept that the lift developed by the screw blades is caused by a circulation flow with strength Γ that takes place around each blade section. The result is decreased local velocity across the blade pressure side and increased local velocity across the suction side. From every point of this bound vortex spring free, trailing vortices, whose strength per unit length is $\partial\Gamma/\partial r$, where r is the distance from the axis of the screw shown in figure 3.3. When the interference flow of this vortex system is small compared with the velocity of the blades, that is, the blades are lightly

loaded, the trailing vortices are approximately helices, and together build a helical or screw surface. When the distribution of the circulation, Γ, is such that, for a given thrust, the energy lost per unit time is a minimum, the flow far behind the screw is the same as if the screw surface formed by the trailing vortices is rigid, and moves backwards in the direction of its axis with a constant velocity [9]. The flow away from the blades is assumed to be continuous and irrotational or without circulation. The circulation around any blade section, in steady flow, is then equal to the discontinuity in the velocity potential at the corresponding point of the screw surface [9]. Goldstein gave a solution for the velocity potential in the fluid domain around blades.

3.2.1 Potential Problem of a Propeller Type Wind Turbine

To solve this problem, assumptions are made that a wind turbine with rotor radius, R, and one blade rotating at speed of Ω operates in a uniform airstream with a velocity V_1. The equation for the trajectory of the screw surface, F, generated by the motion of the blade and the wind is, for $0 \leq r \leq R$,

$$F(z, \theta) = \theta - \Omega \frac{z}{V_1} = 0, \tag{3.10}$$

which is evaluated in a cylindrical polar coordinate system moving at freestream wind speed V_1 as shown in figure 3.3; z is on the rotational axis whose positive direction is downstream from the wind turbine rotor disk and r is the distance from the wind turbine axis. According to the assumptions of minimum energy loss made by Betz [25], the screw surface formed by the trailing vortices is rigid. This screw surface moves downstream in the direction of its axis relative to the undisturbed fluid with a constant induced velocity, v, which can be expressed as

$v = \pm u_a$ where the positive sign is for a screw propeller and a negative sign is for a wind turbine. By imposing the impermeability boundary condition on the screw surface F, the actual velocity of the screw surface in the wake along its rotational axis can be expressed in terms of a velocity potential ϕ,

$$v = \frac{\partial \phi}{\partial z} - \frac{\partial \phi}{r \partial \theta}(\frac{V_1}{r\Omega}) \tag{3.11}$$

for the conditions of $\theta - \omega z/V_1 = 0$, $0 \leq r \leq R$ and $\partial\phi/\partial r \rightarrow 0$ when $r \rightarrow \infty$. This implies that the normal component of fluid speed located on the screw surface is identical with that of the screw surface. As ϕ is a function of r and F [9], the boundary condition of equation 3.11 is manipulated by differentiating ϕ with respect to F,

$$\frac{\partial \phi}{\partial F} = -\frac{\Omega^2 r^2}{V_1^2 + \Omega^2 r^2} \frac{v V_1}{\Omega} \tag{3.12}$$

for $F = 0$ and $0 \leq r \leq R$. For simplicity, let the constant $vV_1/\Omega = 1$, and also let the local tip speed ratio

$$\mu = \frac{\Omega r}{V_1}. \tag{3.13}$$

Equation 3.12 then becomes

$$\frac{\partial \phi}{\partial F} = -\frac{\mu^2}{1 + \mu^2} \tag{3.14}$$

for $F = 0$ and $0 \leq r \leq R$. The velocity potential ϕ should satisfy Laplace's equation $\nabla^2 \phi = 0$ in the fluid domain and this is given by Goldstein [9] in the form of

$$(\mu \frac{\partial}{\partial \mu})^2 \phi + (1 + \mu^2) \frac{\partial^2 \phi}{\partial F^2} = 0. \tag{3.15}$$

This equation should satisfy the boundary conditions of equation 3.11 and also must be a single-valued function of position; its derivatives must vanish when r is infinite and it should be continuous everywhere except at the screw surface. The Laplace equation 3.15 was solved in conjunction with the boundary conditions for

the velocity potential, ϕ, at the discontinuity point $F = 0$ where the screw surface is formed, by Goldstein [9] to give

$$\frac{[\phi]}{\pi} = G(\mu) - \frac{2}{\pi}\sum_{m=0}^{\infty}\left(\frac{\mu_0^2}{1+\mu_0^2}A_m - \epsilon_m\right)\frac{I_{2m+1}(\overline{2m+1}\mu)}{I_{2m+1}(\overline{2m+1}+\mu_0)} \tag{3.16}$$

where

$$G(\mu) = \frac{\mu^2}{1+\mu^2} - \frac{8}{\pi^2}\sum_{m=0}^{\infty}\frac{F_{2m+1}(\mu)}{(2m+1)^2} \tag{3.17}$$

and

$$F_{2m+1}(\mu) = \frac{\mu^2}{1+\mu^2} - T_{1,2m+1}(\overline{2m+1}\mu) \tag{3.18}$$

where,

$[\phi]$ is the velocity potential at discontinuity point;

μ is the local tip speed ratio;

μ_0 is the tip speed ratio;

a_m is the coefficient of the circulation distribution;

A_m is the approximation to the a_m coefficients;

ϵ_m is a correction factor to the approximation coefficient, A_m;

$\overline{2m+1}$ is an algorithm defined by Goldstein [9]

$I_n(x)$ is the modified Bessel function of the first kind;

$T_{1,n}(z)$ is a modified function of a series defined as

$$\begin{aligned} T_{1,n}(z) &= 1 - \frac{n^2}{z^2} + \frac{n^2(n^2-2^2)}{z^4} \\ &\quad - \frac{n^2(n^2-2^2)}{z^6} + \ldots\ldots \end{aligned} \tag{3.19}$$

3.2.2 Calculation of Circulation Distribution

According to the definition in section 3.2.1, the circulation around any blade section is equal to the discontinuity of the velocity potential ,ϕ, at the corresponding point

on the screw surface. Following this definition and restoring the factor Ω/vV_1, temporarily taken as one in the section 3.2.1, the circulation distribution Γ becomes,

$$\frac{\Gamma\Omega}{\pi v V_1} = G(\mu) - \frac{2}{\pi}\sum_{m=0}^{\infty}\left(\frac{\mu_0^2}{1+\mu_0^2}A_m - \epsilon_m\right)\frac{I_{2m+1}(\overline{2m+1}\mu)}{I_{2m+1}(\overline{2m+1}+\mu_0)}. \tag{3.20}$$

The equation 3.20 can also be expressed as

$$\kappa = \frac{1+\mu^2}{\mu^2}\frac{\Gamma\Omega}{\pi v V_1} \tag{3.21}$$

where κ is known as the Goldstein factor which was solved by Goldstein [9] for a two bladed screw propeller and later solved by Tachmindji [27] for three, four, five and six bladed propellers. The factor, κ, is defined as

$$\kappa = \frac{\Gamma B}{\Gamma_\infty} \tag{3.22}$$

where B is the number of blades and Γ_∞ is a circulation for a wind turbine with infinite number of blades. Goldstein's analysis includes tip loss effects for the circulation distribution along the blade span and allows for effects of finite blade number of a rotor.

For infinite number of blades, the circulation distribution Γ at each blade section is

$$\Gamma = \frac{2\pi r u_t}{B}, \tag{3.23}$$

where u_t is the tangential component of induced velocity in the wake and can be expressed as

$$u_t = 2\Omega a' r \tag{3.24}$$

By using Goldstein factor κ, the circulation distribution at each blade section for a wind turbine with finite number of blades becomes

$$\Gamma = \frac{4\pi\kappa r^2\Omega a'}{B}. \tag{3.25}$$

3.3 Application of the Lifting-Line Theory

The circulation distribution of equation 3.25 in section 3.2.2 from the lifting-line theory can be adapted to calculate the performance of a wind turbine with given geometrical characteristics of machines. The wind turbine performance evaluation with both a clean and an iced rotor was done by using this method that was developed by Small and Bose [12,13] and Bose [14].

Figures 3.2 illustrates geometric relations between a wind turbine blade section and the air flow. The geometric pitch angle, ϕ, and advance angle, β, are expressed as,

$$tan\phi = \frac{P_h}{\pi x} \tag{3.26}$$

and

$$tan\beta = \frac{V_1}{\Omega r} \tag{3.27}$$

where P_h is the geometrical pitch and Ω is the rotational speed of the blade. The aerodynamic pitch angle β_i can be expressed in term of advance angle and induced axial and tangential factors as,

$$\begin{aligned} tan\beta_i &= \frac{V_1(1-a)}{\Omega r(1+a')} \\ &= tan\beta\frac{(1-a)}{(1+a')} \end{aligned} \tag{3.28}$$

and

$$tan\beta_i = \frac{\lambda_i}{x} \tag{3.29}$$

where λ_i is an induced advance ratio. The resultant induced velocity should be normal to the incident air flow Lerbs [10], and thus

$$tan\beta_i = \frac{a'\Omega r}{aV_1}. \tag{3.30}$$

From the force diagram in figure 3.4, the local thrust, dT_i, and torque, dQ_i, at a blade element, dr, have the following relation with the aerodynamic pitch angle,

$$tan\beta_i = \frac{dQ_i(\frac{1}{r})}{dT_i}. \tag{3.31}$$

The ideal efficiency for a wind turbine blade element, neglecting the viscous drag force, is

$$\begin{aligned} \eta_i &= \frac{\Omega r}{V_1}\frac{dQ_i(\frac{1}{r})}{dT_i} \\ &= \frac{tan\beta_i}{tan\beta} \end{aligned} \tag{3.32}$$

By combining equations 3.27, 3.28, 3.30 and 3.32, the expression for the induced tangential factor is found to be

$$a' = \frac{tan^2\beta_i(\frac{1}{\eta_i} - 1)}{(1 + tan^2\beta_i)}. \tag{3.33}$$

By applying the Kutta-Joukowski condition at each blade station r, the local lifting force exerted on the blade element dr is

$$dL = \rho V_1 \Gamma dr \tag{3.34}$$

where dL is the lift force at blade station r, and Γ is the circulation distribution along the blade span. Incorporating the Goldstein correction factor, κ, and using equations 3.25 the lift coefficient at each blade element, dr, becomes

$$C_L = \frac{4g\kappa a'}{(1 + a')\sqrt{1 + tan^2\beta_i}} \tag{3.35}$$

where the gap factor g is,

$$g = \frac{\pi x}{B(\frac{C}{D})}. \tag{3.36}$$

in which C is the chord length of the blade element and D is the diameter of the rotor.

The non-dimensional thrust and torque coefficients were defined as

$$K_T = \frac{T}{\rho D^4 n^2} \tag{3.37}$$

and

$$K_Q = \frac{Q}{\rho D^5 n^2} \tag{3.38}$$

where, T and Q are the total thrust and torque of the rotor.

The ideal blade element thrust and torque coefficients k_{T_i}, k_{Q_i} may be calculated as follows. The ideal thrust coefficient was

$$\begin{aligned} k_{T_i} &= \frac{R\frac{dT_i}{dr}}{\rho D^4 n^2} \\ &= \pi^3 x^3 \kappa a'(1+a') \end{aligned} \tag{3.39}$$

and the torque coefficient was

$$\begin{aligned} k_{Q_i} &= \frac{R\frac{dQ_i}{dr}}{\rho D^5 n^2} \\ &= \frac{x}{2} tan\beta_i k_{T_i} \end{aligned} \tag{3.40}$$

In real flow, drag exists due to viscosity of the air and the blade surface roughness. The blade element thrust and torque coefficients were modified by adding the drag force as shown in the force diagram of figure 3.4. This leads to the elemental thrust

$$dT = dT_i + BdDsin\beta_i \tag{3.41}$$

and the thrust coefficient of each element becomes,

$$k_T = (1 + \epsilon tan\beta_i) k_{T_i} \tag{3.42}$$

where the drag-lift ratio $\epsilon = C_D/C_L$. Similarly, the torque coefficient can be expressed as

$$k_Q = (1 - \frac{\epsilon}{tan\beta_i}) k_{Q_i}. \tag{3.43}$$

Finally, overall performance, that is, total thrust coefficient, K_T, torque coefficient, K_Q, efficiency, η, and power ratio, P_r, were found at each tip speed ratio, μ_0, by integrating the elemental values over blade span. Here η is

$$\eta = 2\mu_0 \frac{K_Q}{K_T} \tag{3.44}$$

and P_r is

$$P_r = \frac{P}{P_{Betz}} \tag{3.45}$$

in which P_{Betz} is the maximum possible power absorbed by a wind turbine:

$$P_{Betz} = \frac{8}{27}\pi R^2 \rho V_1^3.$$

which was referred to in section 3.1. This theory is strictly valid for only lightly-loaded rotors where the slipstream expansion is neglected. This assumption is reasonable for a wind turbine working under the cut-out wind speed.

3.4 Computational Method Used for Wind Turbine Performance Evaluation

The performance calculations for horizontal axis wind turbines with both a clean and iced rotor were done by using the lifting-line theory. To assess the wind turbine performance accurately, experimental data for lift and drag coefficients over a wide range of angles of attack were needed. A theoretical curve of lift coefficient was first calculated by using equation 3.35. The real wind turbine operational points were found by matching the theoretical curve with sets of experimental data of lift coefficient and then by obtaining the corresponding drag coefficient. The lift and drag coefficients required were derived from wind tunnel tests for an airfoil used as wind turbine blades and will be described in chapter 4. A computer program that

had been written in FORTRAN was used for this task. This program was initially written by Small and Bose [12,13] for the performance calculation of a wind turbine with a clean rotor and it was adapted for the use of a wind turbine with an iced rotor.

3.4.1 Numerical Process

This program consists of a main program K1 together with subroutines L2, L3, L4, L5, Gold, and Gold3. L2 is a subroutine for initial blade section data input. Gold is a subroutine containing Goldstein correction factors, κ, for two bladed wind turbines; Gold3 provides Goldstein factors for three, four and six bladed wind turbines. The main program K1 integrates the subroutines and the algorithm to calculate a wind turbine's overall thrust coefficient, torque coefficient, efficiency and power ratio over a range of tip speed ratio 0.5 to 12 in 0.5 steps. For each tip speed ratio, the wind turbine blade was divided in 11 radius fractions, 0.1 to 1 in 0.1 steps except at the 0.95 blade station. This program also calculated the aerodynamic properties including induced axial and tangential velocity factors, resultant angles of attack and Reynolds number at each blade element section. The performance of a wind turbine with two, three, four and six bladed rotors can be calculated by incorporating the appropriate Goldstein coefficient for finite number of rotor blades and tip losses.

Within the main program K1, calculations were made first for a theoretical required lift coefficient (equation 3.35) for each blade section over a range of angles of attack from $-6°$ to $90°$ in $2°$ steps. This implied that the induced aerodynamic pitch angle β_i was

$$\beta_i = \alpha + \phi$$

where ϕ is the geometric pitch angle. The operating point of the blade section was the intersection of this calculated lift coefficient curve with the actual section lift coefficient curve found from experimental results. These points were found by using subroutine L3 in which the intersection points of the two curves were derived by systematic comparison of two adjacent points on each of the curves over angles of attack from $-6°$ to $90°$ at two degree intervals. When one value of the theoretical curve fell below the corresponding value on the experimental lift curve, the two curves were considered to be crossed. The $2°$ was then split into 10 and the method repeated to get a closer estimate. The intersection points gave the actual working value of lift coefficient and angle of attack for the blade sections. The actual angle of attack found by the iterative method was then input to the subroutine L4 to derive the drag coefficient from the experimental curve. L5 was a subroutine to recalculate the new theoretical lift coefficient point by the same method used in main program K1 to get a more precise result at the actual operating angle of attack. Goldstein correction factors, κ, were imposed by using subroutines GOLD and GOLD3 for two, three, four and six bladed wind turbines. By using the equations 3.42, 3.43, 3.44 and 3.45 and Simpson's numerical integration method over blade span, the overall performance of the wind turbine including the thrust coefficient, K_T, torque coefficient, K_Q, efficiency, η, and power ratio, P_r, were obtained for both clean and iced rotors. The initial parameters such as blade geometry, including rotor diameter, geometric pitch angle and distribution of chord length along the blade span, and state of rotor, i.e. clean or iced blade were requested by the computer program. A logical flow chart for this computational program is shown in figure 3.5. This program was run in the VAX8530 mainframe computer in the Faculty of Engineering and Applied Science at the Memorial University of Newfoundland.

3.4.2 Calculations for Wind Turbine Models

Prediction of aerodynamic performance degradation for wind turbines with iced rotors under rime and glaze icing conditions were done by using the theory and numerical method described above. The program computed wind turbine performance including K_T, K_Q, η and P_r as well as power reduction over tip speed ratio 0.5 to 12, but for conciseness only the results of power ratio are displayed.

Two designs of wind turbine were studied. One was a two-bladed small wind turbine with 2.5 m diameter rotor, linear twisted blades and uniform blade chord length along blade span. The other was a Carter-23 two-bladed wind turbine with 23 m diameter rotor, non- linear blade twist and non-linear blade chord length. Both machines were assumed to have the same LS(1)-0417 airfoil blade section and operated at a uniform wind speed of 10 m/sec. Wind shear effects and wind turbulence were neglected in this computation.

The wind turbines were assumed to be operating in typical rime or glaze icing conditions. Figures 3.6 to 3.11 are calculated results of power ratio for the 2.5 m rotor wind turbine and the Carter-23 wind turbine at different atmospheric icing conditions. Results show that the effect of rime icing on the wind turbine's blades were not as severe as that of glaze icing; glaze icing almost completely destroyed both wind turbines' aerodynamic performance. Rime icing reduced power output for the Carter-23 wind turbine by 30% and for the 2.5 m rotor diameter wind turbine by 49% over a range of tip speed ratios from 0.5 to 12.

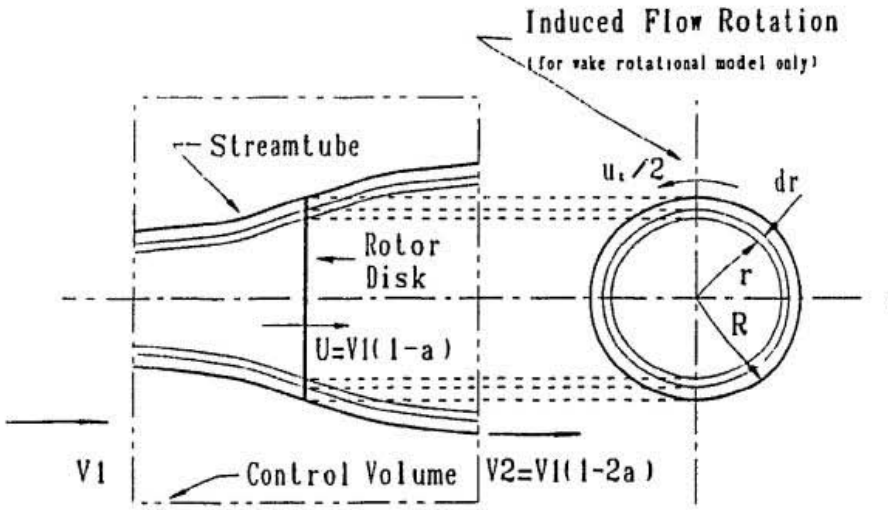

Figure 3.1: Stream tube for momentum theory.

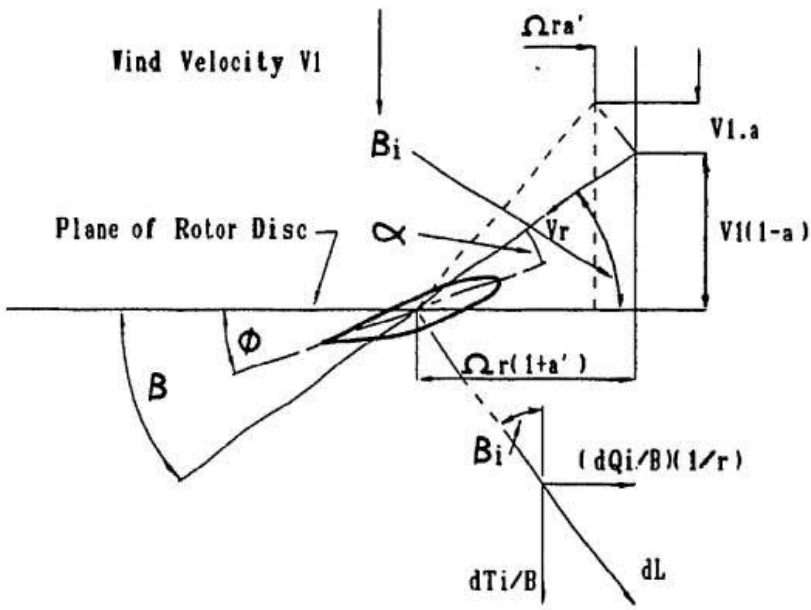

Figure 3.2: Velocity diagram at blade section *dr*.

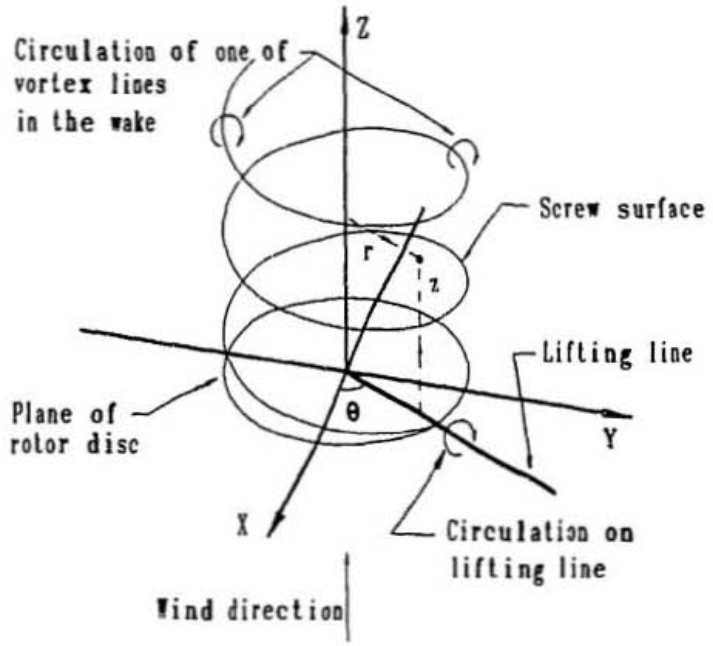

Figure 3.3: Coordinate of wind turbine screw surface in the wake.

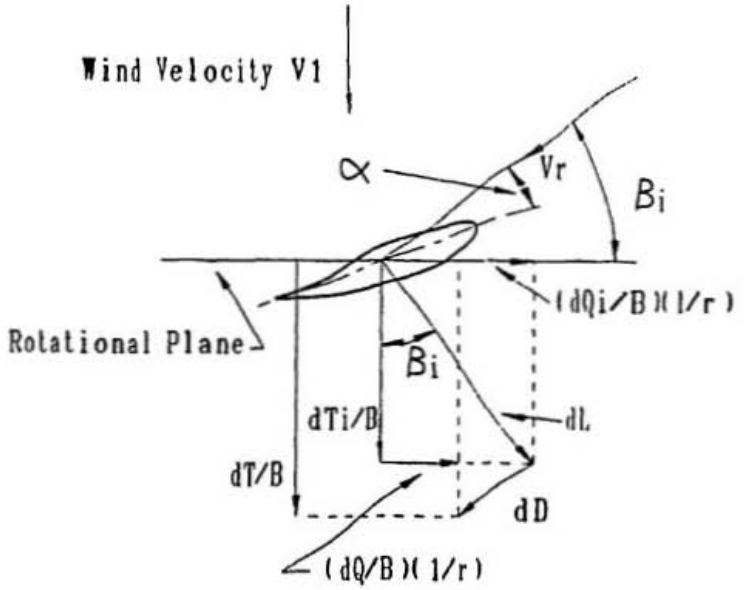

Figure 3.4: Force diagram at blade section dr.

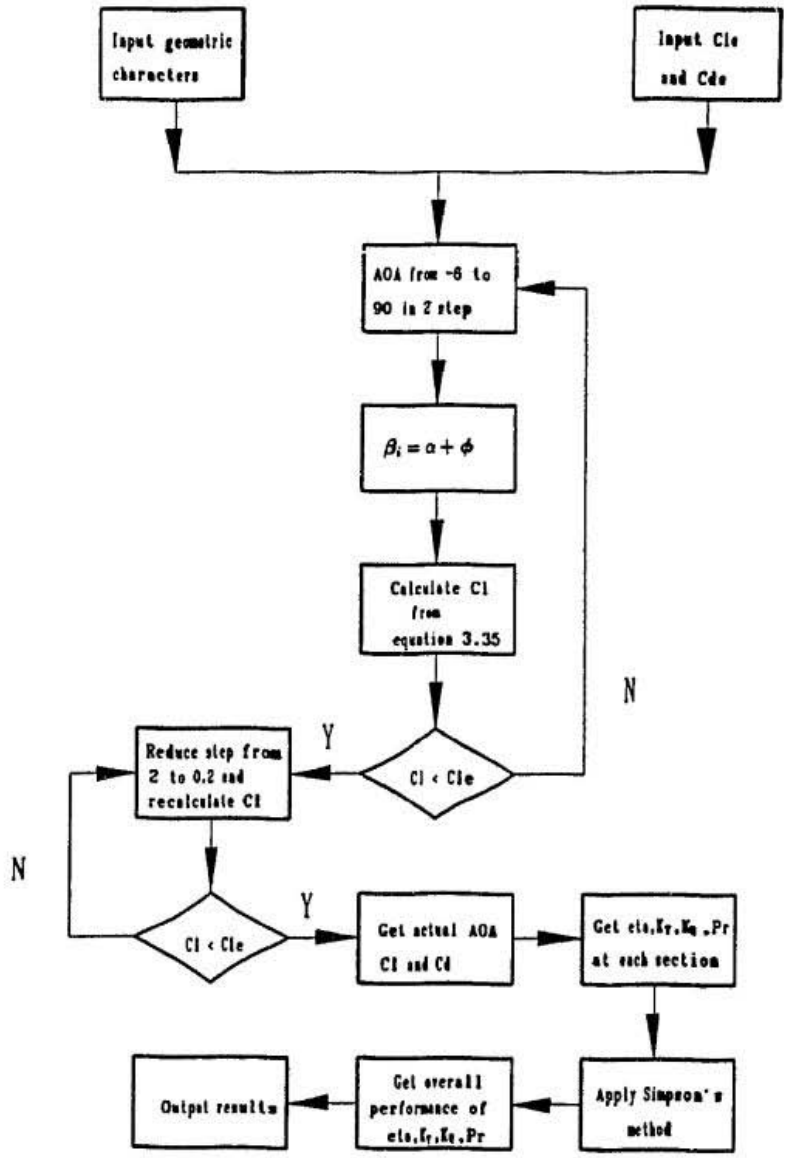

C_{le}: Experimental lift coefficient
C_{de}: Experimental drag coefficient

Figure 3.5: Flow chart for K1 program.

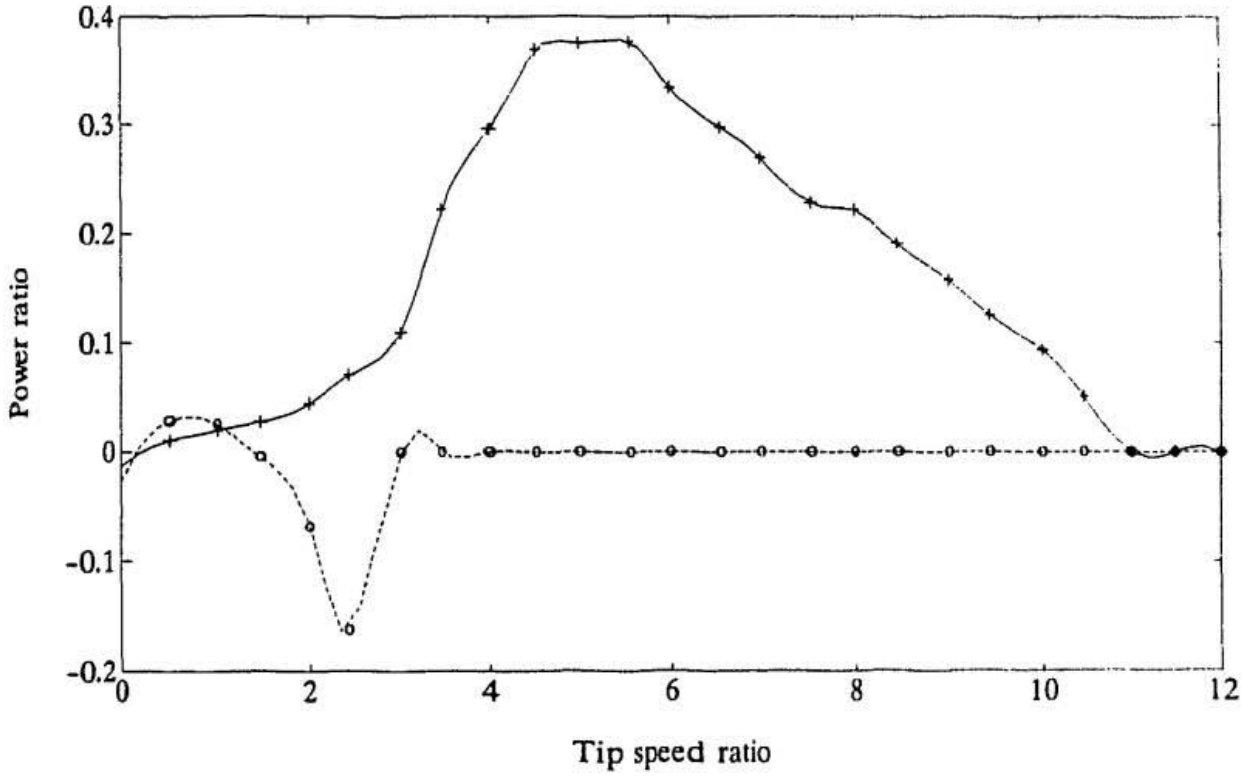

'*': Clean wind turbine
'o': Glazel iced wind turbine

Figure 3.6: Computed results of power ratio for the 2.5 m diameter horizontal axis wind turbine.

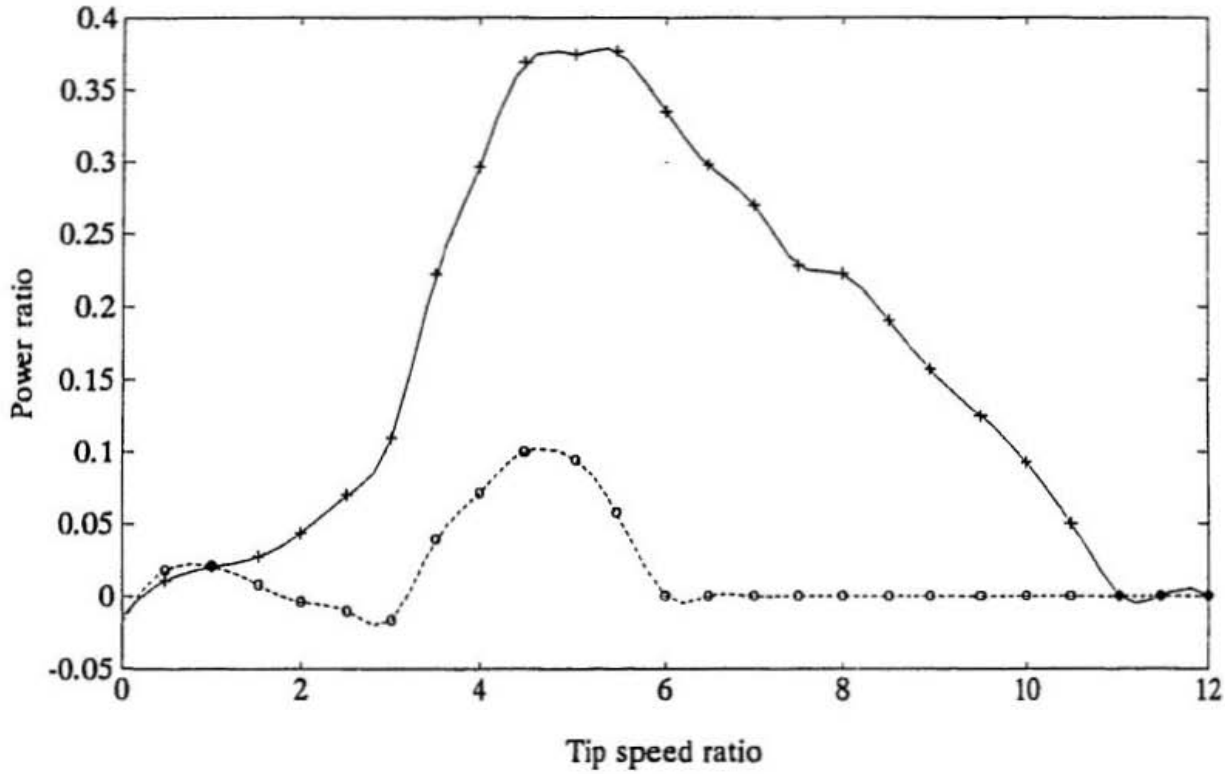

'*': Clean wind turbine
'o': Glaze2 iced wind turbine

Figure 3.7: Computed results of power ratio for the 2.5 m diameter horizontal axis wind turbine.

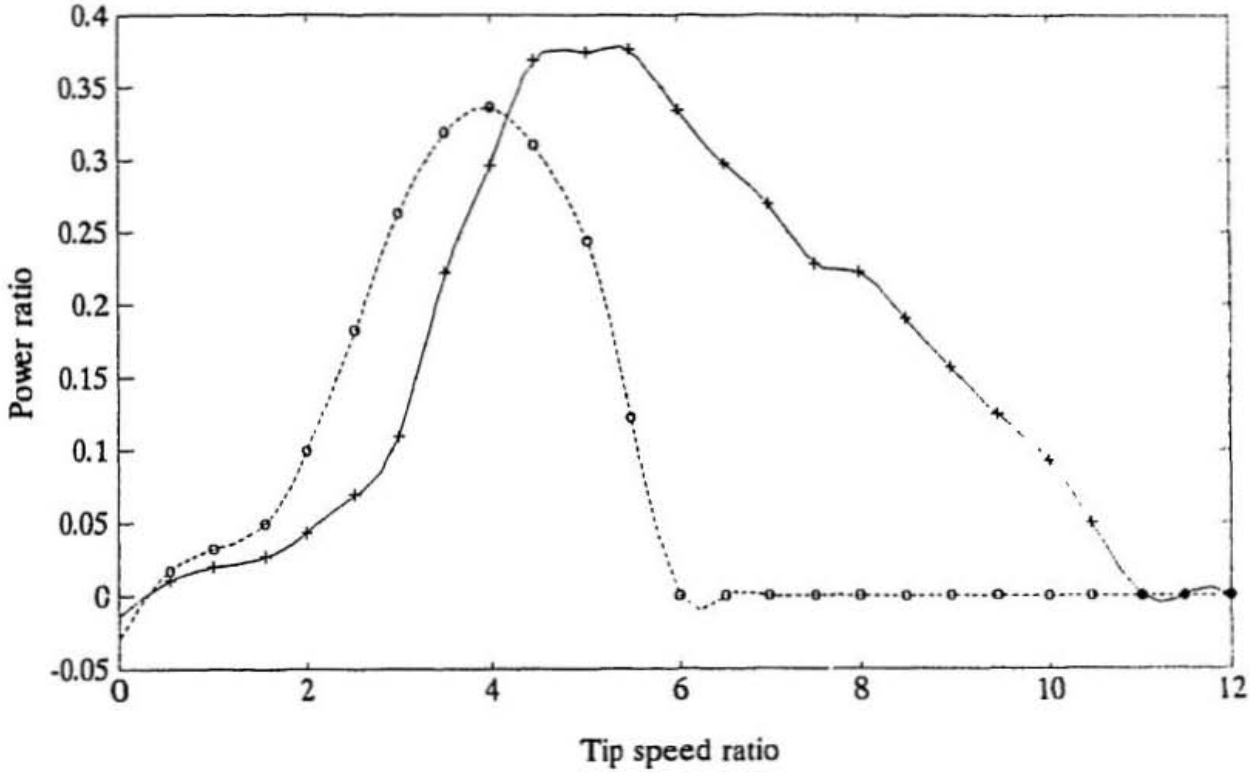

'*': Clean wind turbine
'o': Rime iced wind turbine

Figure 3.8: Computed results of power ratio for the 2.5 m diameter horizontal axis wind turbine.

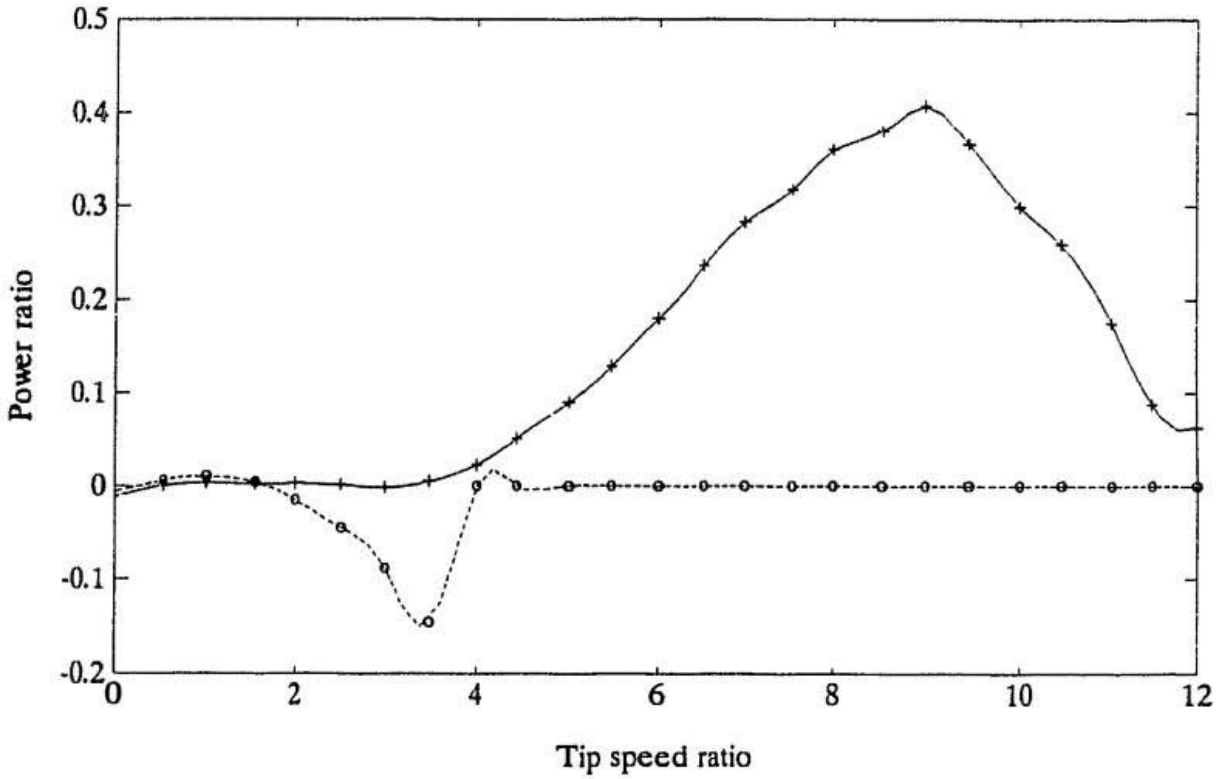

'*': Clean wind turbine
'o': Glaze1 iced wind turbine

Figure 3.9: Computed results of power ratio for Carter-23 wind turbine.

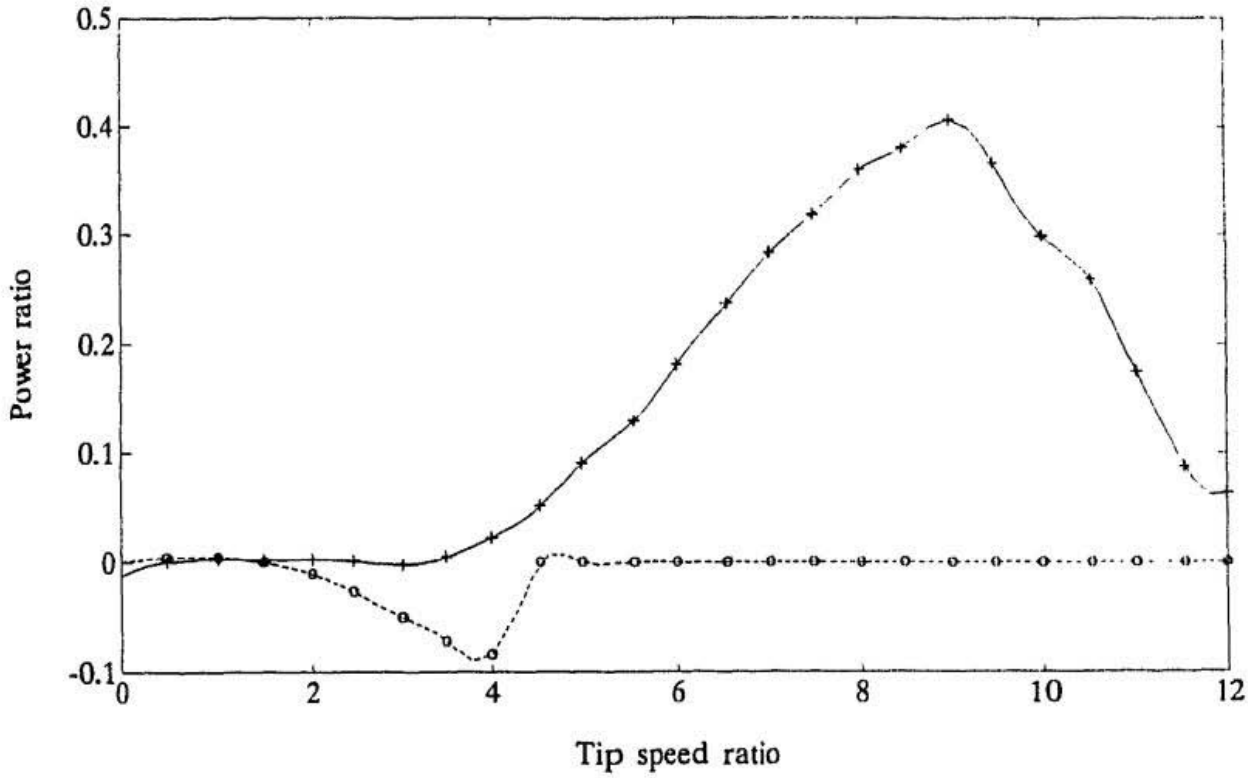

'*': Clean wind turbine
'o': Glaze2 iced wind turbine

Figure 3.10: Computed results of power ratio for Carter-23 wind turbine.

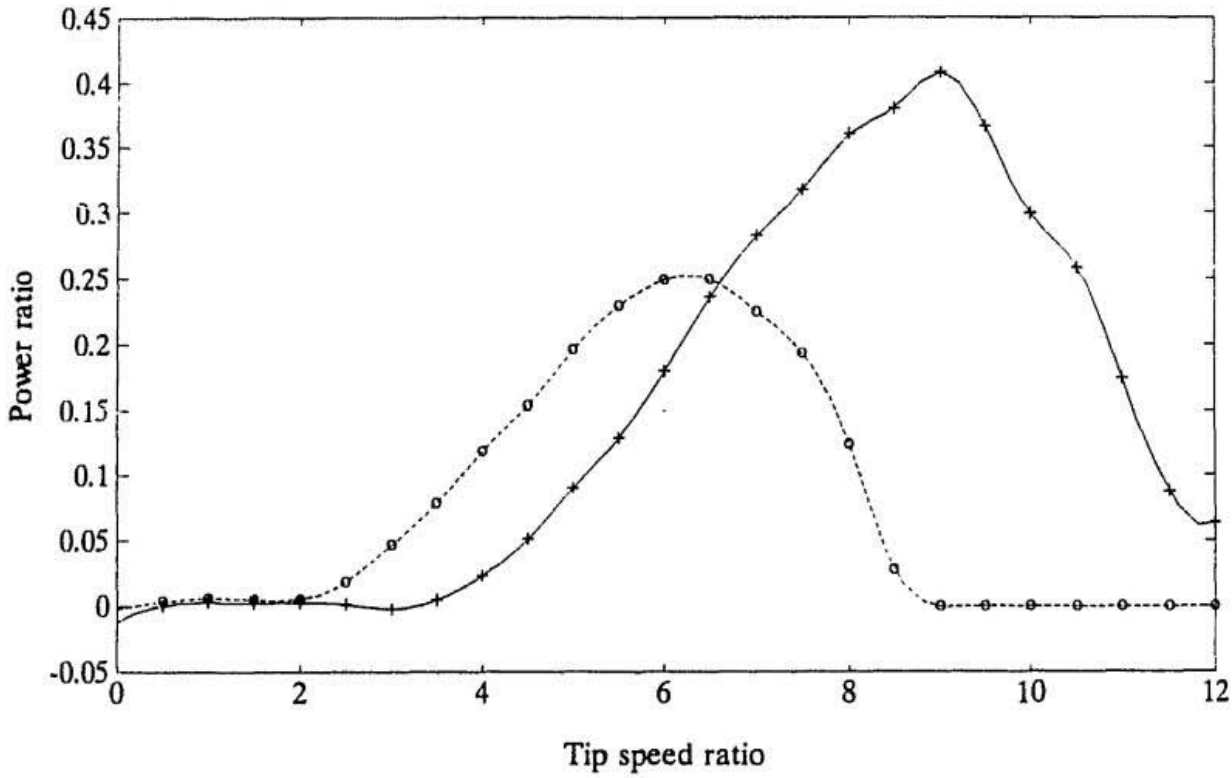

'*': Clean wind turbine
'o': Rime iced wind turbine

Figure 3.11: Computed results of power ratio for Carter-23 wind turbine.

Chapter 4

Wind Tunnel Tests for Airfoil with Simulated Ice Deposits

Until recently, very little experimental data has been available on the performance degradation of airfoil sections resulting from rime or glaze ice accretion over wide ranges of angles of attack. During the past 10 years, most theoretical and experimental work has been focused on two aspects: the evaluation of degradation of aerodynamic performance for an airfoil in aircraft cruise or climbing conditions due to ice accretion; and the conduct of icing and de-icing tests for rotors of helicopters.

Bragg [28,29] investigated the effects of simulated ice shapes on lift, drag and pitching moment of an airfoil section in aircraft cruise conditions; that is for angles of attack in or below the stall region. He also provided information on the length of separation bubbles, reattachment and trailing edge separation. Bragg and Coirier [30] simulated glaze ice accretion on a 21 inch chord model of a NACA 0012 airfoil and reported measurements of surface pressure, lift, drag and moment coefficients over a range of angles of attack in and below stall. Model scale helicopter rotor icing tests were done by Guffond et al. [31]. Ice shapes that accumulated on the rotor blades during icing tunnel tests were documented and studied at different

Mach number under different atmospheric conditions as well as the effects of the performance of the rotor due to icing.

Computational means have also been developed to model the flow over an iced airfoil. Cebeci [32] used an interactive boundary layer technique to predict the aerodynamic characteristics of an airfoil with leading edge ice accretion. Potapczuk [33] used a parabolized Navier-Stokes model to make a similar calculation. Bragg [16] predicted the performance of a NACA 0012 airfoil with simulated glaze ice accretion and compared this with that predicted by the NASA Lewice ice accretion computer code for the same icing conditions; results of both the interactive boundary layer model and the Navier-Stokes method were compared with experimental data. Numerical simulations were also made for helicopter blade icing by Oleskiw [34] to simulate the rime ice accretion process on the rotor blades. Potapczuk and Berkowitz [35] presented experimental data for a Boeing $737-200ADV$ wing section for a range of angles of attack from $-2°$ to $20°$. These data were collected under glaze, rime and glaze-rime mixture icing conditions for an airfoil of 16 inch chord.

Although considerable research has been done on atmospheric icing, performance tests of an iced airfoil over a wide range of angles of attack are rare and very little experimental data has been found in the literature on iced airfoils over this wide range, that is, angles of attack from $-6°$ to $90°$. This restricts the application of the theoretical method described in chapter 3 for evaluation of performance degradation of wind turbines under icing conditions as the method is largely dependent upon experimental section data over a range of angles of attack from $-6°$ to $90°$.

This chapter describes tests on an airfoil in a wind tunnel, whose section geom-

etry corresponded to the airfoil section used as the blades of a rotor. Testing was performed in a low speed wind tunnel at Memorial University of Newfoundland. The tested airfoil model was a NASA LS(1)-0417 wing section. Various simulated iced shapes that were recorded from previous tests [5] and from other documents [15,16] were tested. The simulated ice shapes were made from wood in a model shop in the Faculty of Engineering and Applied Science at Memorial University of Newfoundland. An Aerolab balance dynamometer table was used to support the model and measure the aerodynamic forces exerted on the wing. A Keithley S575 data acquisition system and a hot wire anemometer were used to measure aerodynamic forces exerted on the airfoil and the wind velocity inside the wind tunnel.

4.1 Calibration of Wind Tunnel Working Section

The layout of the low speed wind tunnel, which is located in the Fluids Laboratory in the Faculty of Engineering and Applied Science, is shown in figure 4.1. This wind tunnel is 10 m long; it has a cross section of 1m × 1m. Section one is a boundary layer testing section and section 2, which was used for the airfoil tests, is upstream of section one and provides space where non-boundary layer tests can be conducted. The maximum wind speed that could be provided by the wind tunnel at this location was about 14.5 m/sec.

4.1.1 Calibration of the Hot-Wire Anemometer

A Disa hot-wire constant temperature anemometer (CTA) was calibrated before the wind tunnel tests were done. The hot-wire or hot film anemometer is at present the most widely used measuring system for analysis of velocities in turbulent flow.

The Disa $55M01$ anemometer is a multipurpose instrument primarily used for measurements of the instantaneous mass flow of a gas or liquid; it uses as a transducer either a hot-wire or a hot-film probe. The instrument has a build-in DC meter for measurement of probe cold resistance and for indication of mean flow. Based on measuring the convective heat loss from the electrically heated hot-wire/film sensor caused by the flow of gas or liquid surrounding the sensor, the fluid velocity can be measured. A P11 single hot-wire sensor from Dantec was used; this consisted of a 5μm diameter platinum-plated tungsten wire. Wires are suspended between two prongs, to which they are welded. The probe was placed at the centre of the tunnel working section. The anemometer was adjusted to have optimum frequency response by using a built in square wave generator with different frequencies. Values of standard flow velocities at the working section of the wind tunnel were obtained by using a pitot-tube. A set of 20 points of wind velocity samples were collected by controlling air flow at the inlet of the wind tunnel fan. Dantec Acqwire data acquisition software was used to process the calibration data.

4.1.2 Wind Tunnel Calibration

The ideal flow field provided by a wind tunnel for an airfoil test should be uniform with low turbulence intensity across the tunnel working section. Non-uniform flow can cause distortion of the loads exerted on the tested body. Flow with higher turbulence intensity can change the position of transition to turbulent flow on the suction side of the model and, therefore, change the drag and maximum lift. The quality of the flow field in the working section had to be examined before tests proceeded.

A two degree of freedom motion traverse was designed to support the probe so

that the sensor could be positioned everywhere across the tunnel working section through a cantilever. Figure 4.2 shows points measured across wind tunnel section. The wind speed and turbulence intensity at each point were measured and are shown in appendix in page 100. The results show that beyond the wall boundary layer, the maximum turbulence appeared at point G_7 and was about 4%; the turbulence was much lower towards the centre of the working section. The definition of the flow turbulence intensity, u_{ti}, used was,

$$u_{ti} = \frac{u_{rms}}{U_m} \times 100, \tag{4.1}$$

where U_m is the mean value of the wind speed and u_{rms} is the root mean square or the standard deviation defined as

$$u_{rms} = \sqrt{\frac{1}{N}\sum_{n=1}^{N}(U(n) - U_m)^2} \tag{4.2}$$

in which U is wind velocity measured and N is the number of samples. The low turbulence intensity and low mean velocity variations across the working section provided good conditions for the airfoil tests.

4.2 Calibration of the Strain Gauged Balance Table

An Aerolab Pyramidal Strain Gauged Balance System was used to support the model in the wind tunnel. This device is shown in figure 4.3. Its angles of attack could be adjusted over a range of ±25 degree and its angle of yaw over a range of 360 degrees. It was possible to measure six force and moment components which fully determined the resultant force exerted by the airstream on the airfoil. A mounting adaptor was fixed on the mounting plate at the top of the balance

table to change the range of angles of attack from previous ±25 degree to -10 to 36 degrees. The ranges of angle of attack were extended further to 90 degree at a lower tunnel velocity of 6m/sec; this restriction on wind speed was due to the capacity limitation of the balance table. The force components were separated mechanically and measured through individual strain gauged load cells. The signal from each strain gauge was amplified by a strain gauge amplifier and then sent to a micro computer. A Keithley S575 data acquisition unit was used to process the signals. The average value of each component was found by use of a program which took the mean of the data points corrected.

From the figure 4.3, the basic linkage on the balance table may be termed a pyramidal linkage. The central spider which carried the spindle was supported on four diagonal struts which, if extended, would meet at a point known as the balance centre. The balance table was calibrated before set up beneath the wind tunnel. Force calibration was done by using a 10 inch diameter pulley that could turn freely on a ball bearing without much resistance. Loads of 0.5, 1, 5, 10, 20, 40 lbs were applied to check the linearity of the strain gauges and 0.5 up to 90 lbs.in for the moment. The calibrated data of force and moment were sent to the computer to get polynomial force and moment functions for the calibrations. As all the calibrations of the components were about the balance centre and the stem used to support the model had a 0.4 m difference in height from the balance centre to the point at which the airfoil was attached and as a mounting adapter was used to change the range of angles of attack from ±25 degree to the range of −10 to 90 degree, correction was made for the component of pitch moment from the force balance by adding the extra moment resulting from the displacement between the mounting centre and the rotational centre .

4.3 Test Procedure and Results

The airfoil tested was a NASA LS(1)-0417 wing section with a 0.2 m chord length and a 0.8 m span: i.e. an aspect ratio of four. This blade section was the same family as the blade sections used for the Carter WEC-23 wind turbine. The offsets of the profile of this airfoil are shown in table 4.1. This model was made from aluminium alloy(H6061) and it was manufactured on a CNC machine at the University of Victoria.

The airfoil was mounted on the top of the mounting bar of the dynamometer inside the wind tunnel as shown in figure 4.4. Each channel signal from the strain gauges was set to zero before each test to reduce the effects of zero drift from the amplifiers. Signals from the strain gauges on the dynamometer for each force component were sent to a multi channel strain gauge signal amplifier. Figure 4.5 shows the instrumentation for the wind tunnel test.

Several tests were performed for the clean airfoil and for the airfoil with various simulated ice profiles. Three ice accretion shapes were simulated. The glaze 1 ice deposit shown in the figure 4.6 was obtained from a 5 minute duration icing test on a wind turbine model that is described in the next chapter; the glaze 2 ice profile shown in figure 4.7 was from the NASA Lewis research centre [16] under icing conditions of temperature $-7°C$, liquid water content $2.18 g/m^3$, wind speed 57 m/sec and droplet diameter $20\mu m$; the rime ice profile shown in figure 4.8 was from Wilder [15]. The ice profiles were traced and simulated by using a specially shaped wood strip. Each simulated ice profile was attached to the leading edge of the airfoil by using double-sided sticky tape so that these could be fastened and removed easily. Plasticine was used to seal gaps between the airfoil and simulated

ice accretion. A hot wire sensor, which was fixed on a cantilever, was placed upstream of the model. The wind velocity within the chamber was set to 6 m/sec for range of angle of attack of $-6°$ to $90°$.

Figures 4.9 to 4.14 show the test results of lift and drag coefficients for the clean airfoil and airfoil with glaze 1, glaze 2 and rime ice shapes. Tests were done for steps of $2°$ angles of attack except at angle of attack of $15°$ for the clean airfoil, where the maximum lift coefficient appeared.

Due to the capacity limitation of the dynamometer, the wind velocity was set to 6 m/sec for the full range airfoil tests i.e. the ranges of angle of attack from -6 to 90 degree.

In the clean airfoil test, the model was stable until an angle of attack of $16°$ was reached where the airfoil stalled with an abrupt drop in the lift coefficient and increase in the drag coefficient. Due to a lack of rigidity of the support bar, mounting plate and the balance table itself, the separated turbulent flow on the back of the airfoil forced the model to vibrate. This vibration could induce additional flow turbulence around the airfoil and affected the test results beyond the stall region to some extent. The simulated glaze 1 ice profile test showed that even at low angles of attack, for example $0°$, flow separation occurred behind the two 'horns' of the ice shape and the flow around the surface of the airfoil was turbulent, and this induced some vibration of the model. The significantly altered shape of the airfoil as a result of the icing caused the streamlined flow around the surface of the airfoil to break down even at low angles of attack. This was associated with a decrease of lift and increase in pressure drag. The rime ice accretion test showed that no significant change of the airfoil performance took place, except around the point of maximum lift coefficient, where there was a slight drop of lift coefficient.

Discussions of the results is given in chapter 6.

Due to finite aspect ratio of the airfoil and the blockage effect on the aerodynamic properties, the data from figures 4.9 to 4.14 has been corrected in the manner described below.

4.4 Tunnel Interference Effects and Data Correction

The object of the wind tunnel tests on the airfoil model was to obtain the airfoil performance in open air conditions. As a result of distortion of the flow pattern due to the limited cross section of the tunnel and because the model airfoil had a finite span, the raw test data did not correspond to the airfoil performance of a 2-D airfoil in open air and had to be corrected.

4.4.1 Blockage Correction

A. Solid blockage correction

In the case of a closed wind tunnel, if the working section has straight rigid boundaries, continuity of mass flow in the tunnel requires that the axial velocity in the vicinity of the model must exceed the value well upstream which is the so called tunnel velocity U_T. This gives an expression in terms of a blockage factor ϵ,

$$U_F = U_T(1 + \epsilon), \tag{4.3}$$

where U_F is the wind speed corresponding to the open air speed that is taken to be the speed in the tunnel at the position of the model.

Solid blockage ϵ_s in two-dimensional flow was determined by Lock [36]. This investigation was done by considering the wing as a doublet located at the position

of the model and of such strength as to produce the same velocities in the far field as are produced by the airfoil itself. The boundaries of the working section of the tunnel were then represented by image systems of the equivalent doublet instead of the airfoil itself and the solid blockage was calculated as the velocity induced at the position of the model by the image doublets [36].

For a wing with maximum thickness, t, placed between the roof and floor of a wind tunnel of height h and completely spanning the breadth, b, the value of solid blockage correction, ϵ_s, is given by the expression

$$\epsilon_s = \tau\lambda(\frac{t}{h})^2 \tag{4.4}$$

where

$$\tau = \frac{\pi^2}{12}(1 + \frac{3\pi^2 a^2}{4h^2}) \tag{4.5}$$

in which a is the distance between the model and the tunnel axis if the wing is not symmetrically placed between the roof and the floor, h is the tunnel section height and λ is the body factor that depends on the geometry of the basic shape of the airfoil,

$$\lambda = \frac{4}{\pi}\int \frac{q}{U} y \frac{ds}{t^2} \tag{4.6}$$

where q is the local velocity at the surface at a distance s from the leading edge measured along the surface, U is the free air speed and y is the distance from this point to the chord line. The integral is taken over the upper surface of the symmetrical section from the leading edge to trailing edge. For a modified Joukowski airfoil profile with a thickness ratio t/c of six, the value of λ is found to be three [36]. These data were applied to the NASA LS(1)-0417 airfoil. For a more general case of the solid blockage of an airfoil at an angle of attack, α, the body factor λ

should be increased by the amount $K_1\alpha^2$ where K_1 is a function of t/c which was presented by Pankhurst and Holder [37].

B. Wake blockage correction

The total head of the fluid in the wake of a body is less than that in the region outside the wake due to energy dissipation. As the static pressure in a tunnel is practically constant across any given section normal to the stream, it follows that the dynamic head, and hence the velocity, in the wake of the model must be lower than in the surrounding stream. Therefore, in order to satisfy the condition of continuity of mass flow, the velocity of the fluid outside the wake must exceed the velocity far upstream of the model. Thus the axial velocity in a wind tunnel gradually increases past the model except for the reduced velocity inside the wake, and the velocity at the position of the model is correspondingly greater than the tunnel speed. It was suggested by Glauert [38] that for a wing completely spanning a closed tunnel, a wake blockage factor ϵ_w could be expressed as

$$\epsilon_w = \eta \frac{t}{h} \tag{4.7}$$

where η is an empirical factor. For a similar Joukowski section with a thickness ratio of six, η is given as 0.08 [38].

The total blockage correction factor, ϵ, was calculated as

$$\epsilon = \epsilon_s + \epsilon_w \tag{4.8}$$

and the apparent force coefficient C_{FT} can be expressed as a corrected value $(C_F)_F$ corresponding to the value in an open air stream,

$$(C_F)_F = C_{FT} \frac{1}{(1+\epsilon)^2} \tag{4.9}$$

4.4.2 Correction for Finite Aspect Ratio

Finite aspect ratio of the airfoil causes the flow field around the airfoil to be no longer two dimensional; streamwise vortices are shed from the trailing edge of the airfoil and these result in the generation of an induced velocity at each blade station across the blade span. The induced drag and the circulation distribution along the airfoil vary depending on the position of the airfoil section and the circulation reaches zero at the two airfoil tips. The drag coefficient obtained from the model test for finite aspect ratio, A, were converted to an equivalent two-dimensional value by the equations

$$C_{DO} = C_D - \frac{1}{\pi A}(1+\delta)C_L^2 \tag{4.10}$$

and

$$\frac{1}{a_o} = \frac{1}{a} - \frac{1}{\pi A}(1+\tau) \tag{4.11}$$

where C_{DO} is the drag coefficient for infinite aspect ratio, C_D is a drag coefficient for finite aspect ratios, a and a_o are the slope of the lift coefficient curves for finite and infinite aspect ratio respectively and δ, τ are constants. Both a for finite aspect ratio of four and a_o for two dimensional flow were given by Glauert [38] as 4.04 and 2π respectively. The conversion factor, F_L, for change of the lift coefficient from three dimensional to two dimensional flow was obtained by taking the ratio a/a_o.

The original test data were then input into a computer program called COR.FOR and were corrected by using the algorithm above.

There is much difference of performance degradation effected by glaze and rime icing. The wind tunnel test results illustrated in figures 4.9 to 4.14 showed that a dramatic decrease of lift coefficients and increase of drag coefficients occurred when glaze icing accreted on this airfoil section even if the angles of attack were

low. Rime icing had less effect on the airfoil performance, even though the rime icing had approximately the same quantity of ice as the glaze ice profile as shown in figures 4.7 and 4.8. Glaze ice formation destroyed the streamlined shape of the airfoil so that severe aerodynamic degradation resulted. Detailed discussion is presented in chapter 6.

Once the airfoil section data over a wide range of angles of attack were obtained, the wind turbine performance evaluations in different atmospheric icing conditions could proceed and these are described in chapter 3.

Figure 4.1: Layout of low speed wind tunnel.

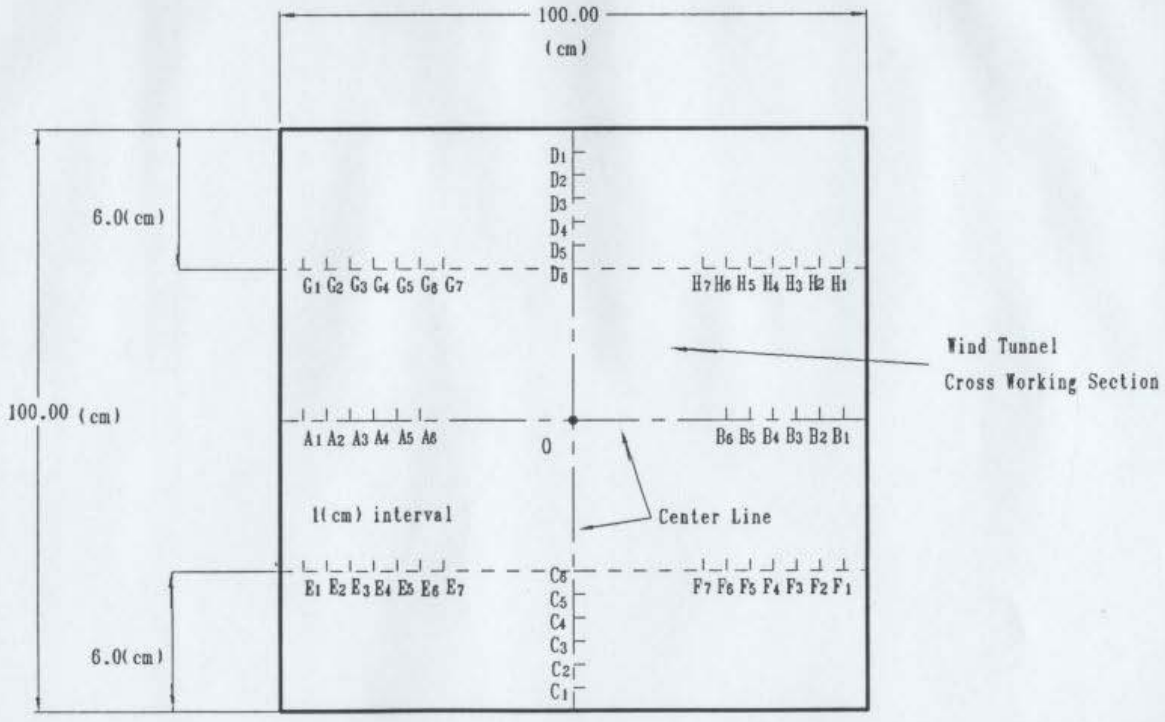

Figure 4.2: Wind tunnel cross section and distribution of calibration points.

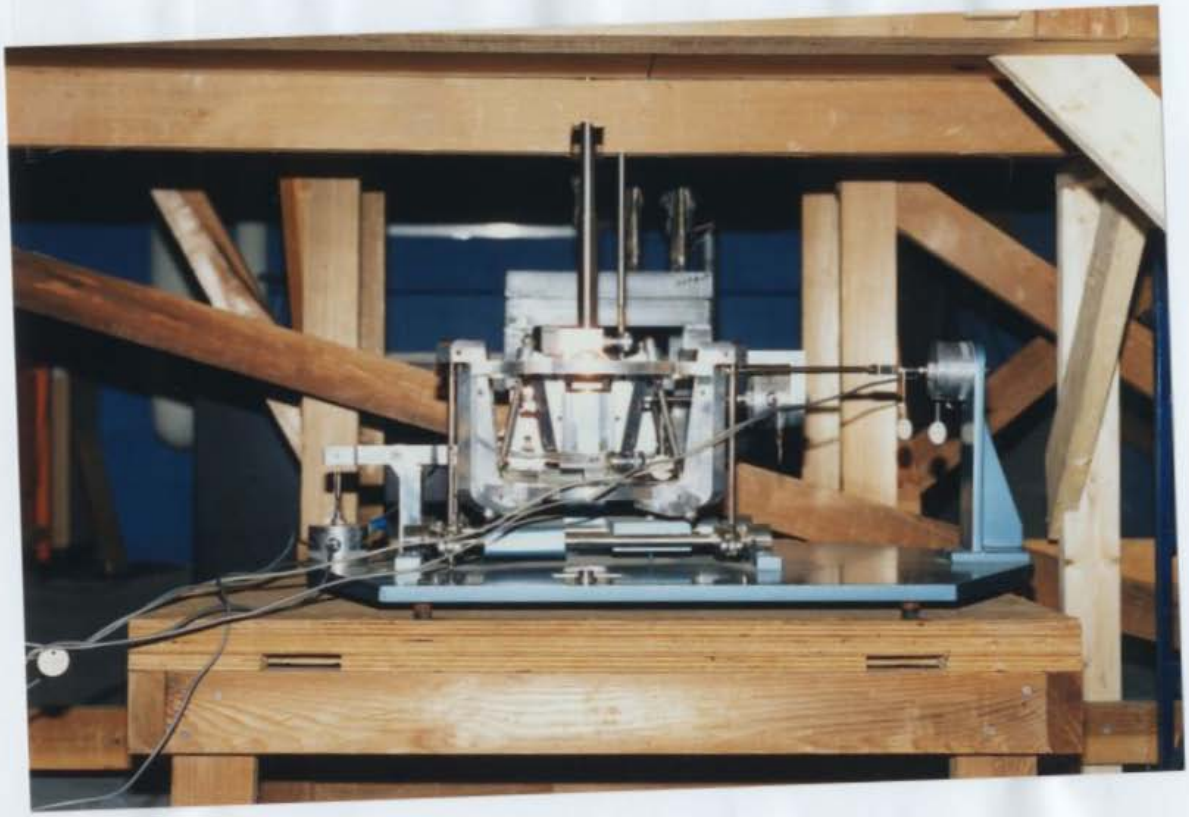

Figure 4.3: Dynamometer for the airfoil test.

Figure 4.4: Installation of airfoil on top of mounting bar.

Figure 4.5: Instrumentation for the wind tunnel tests.

Figure 4.6: Simulated glazel ice shape.

Figure 4.7: Simulated glaze2 ice shape.

Figure 4.8: Simulated rime ice shape.

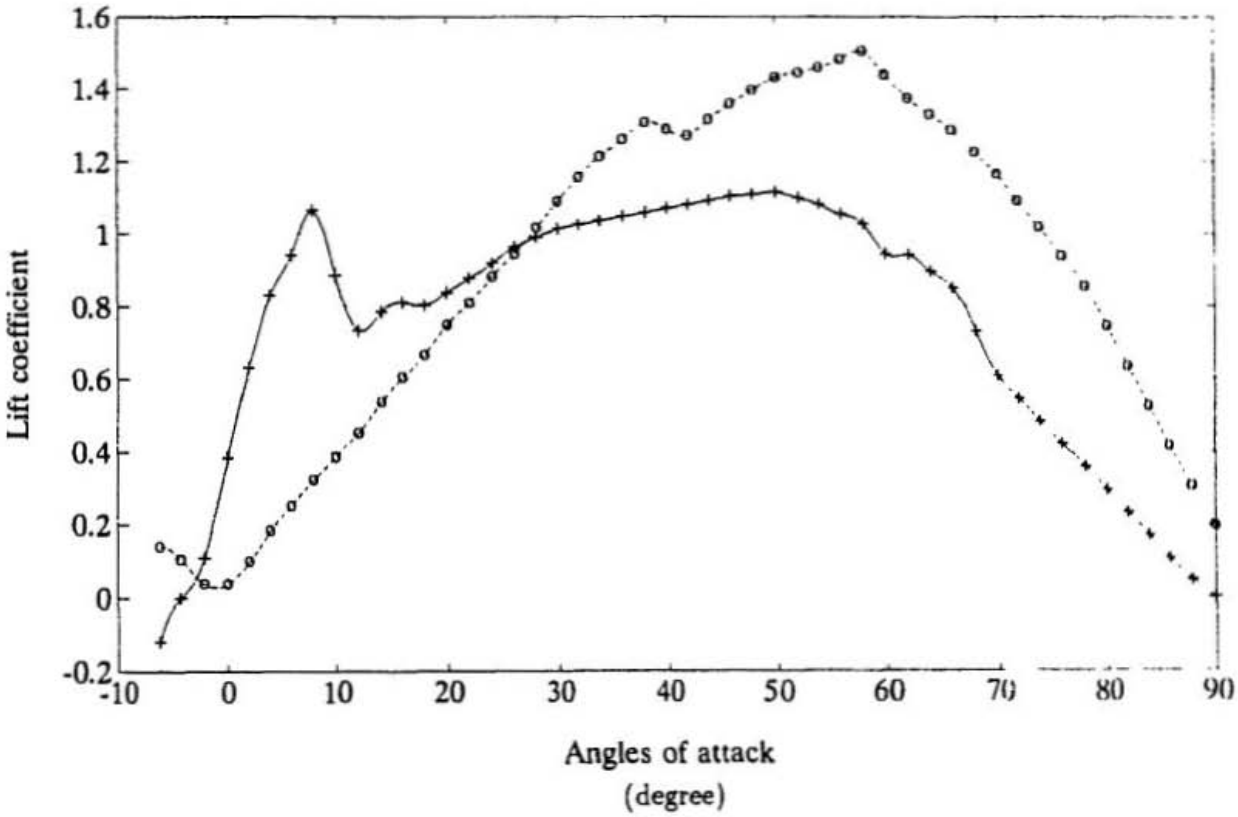

'*': Clean airfoil
'o': Iced airfoil

Figure 4.9: Test results of lift coefficient for NASA LS(1)-0417 clean and glazel iced airfoil.

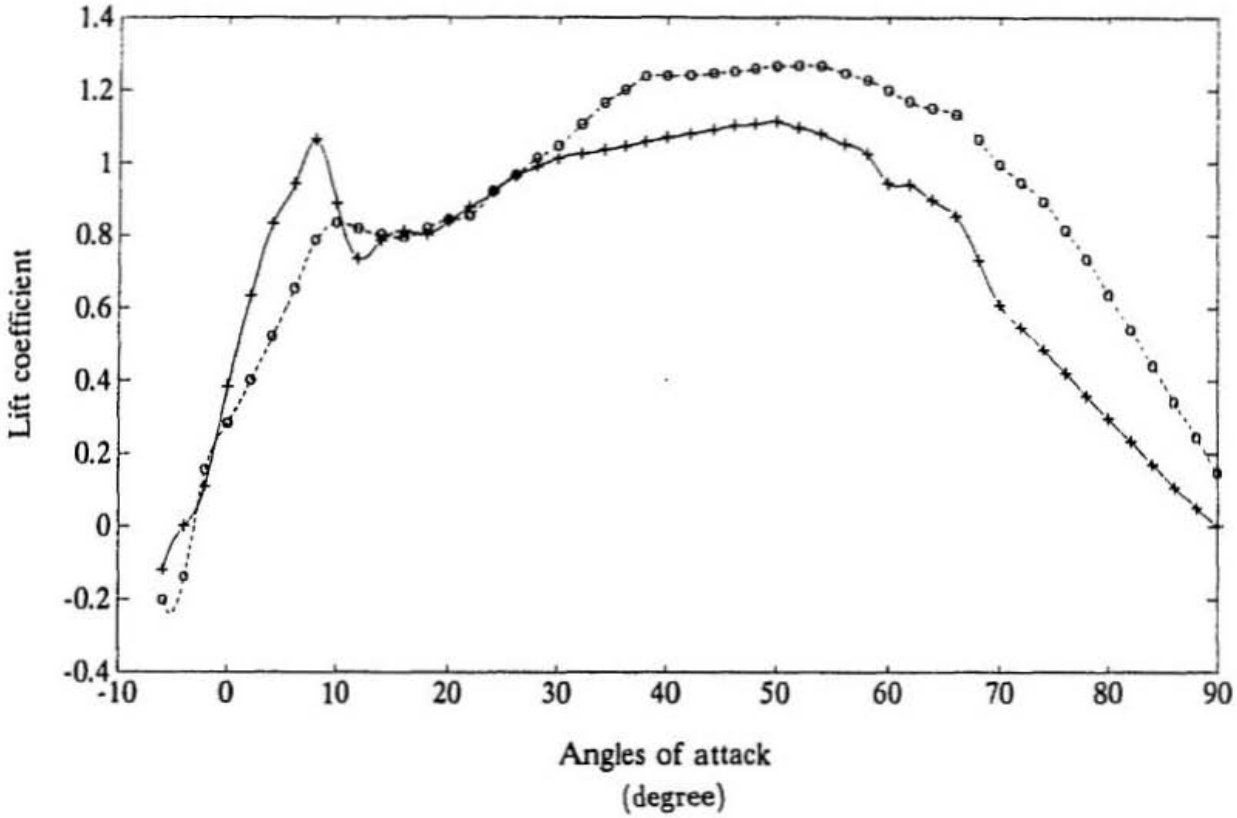

'*': Clean airfoil
'o': Iced airfoil

Figure 4.10: Test results of lift coefficient for NASA LS(1)-0417 clean and glaze2 iced airfoil.

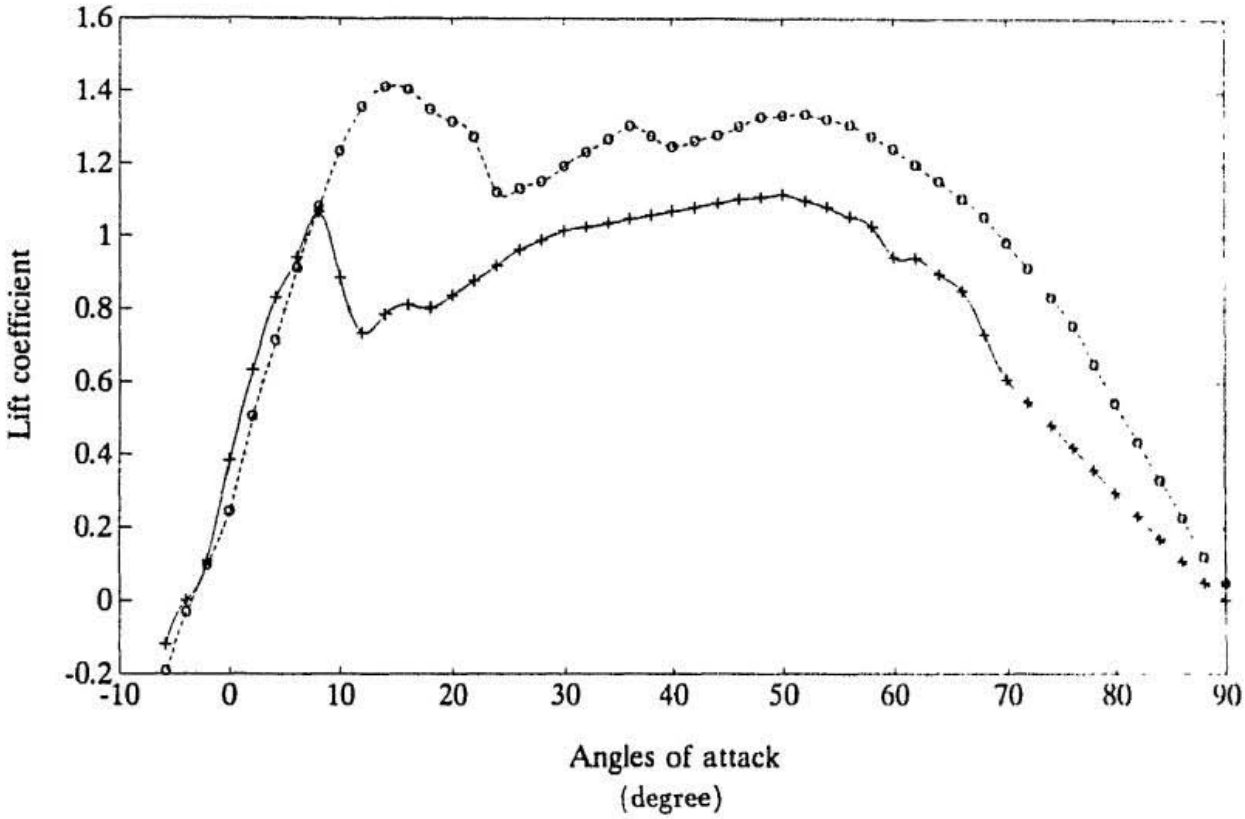

'*': Clean airfoil
'o': Iced airfoil

Figure 4.11: Test results of lift coefficient for NASA LS(1)-0417 clean and rime iced airfoil.

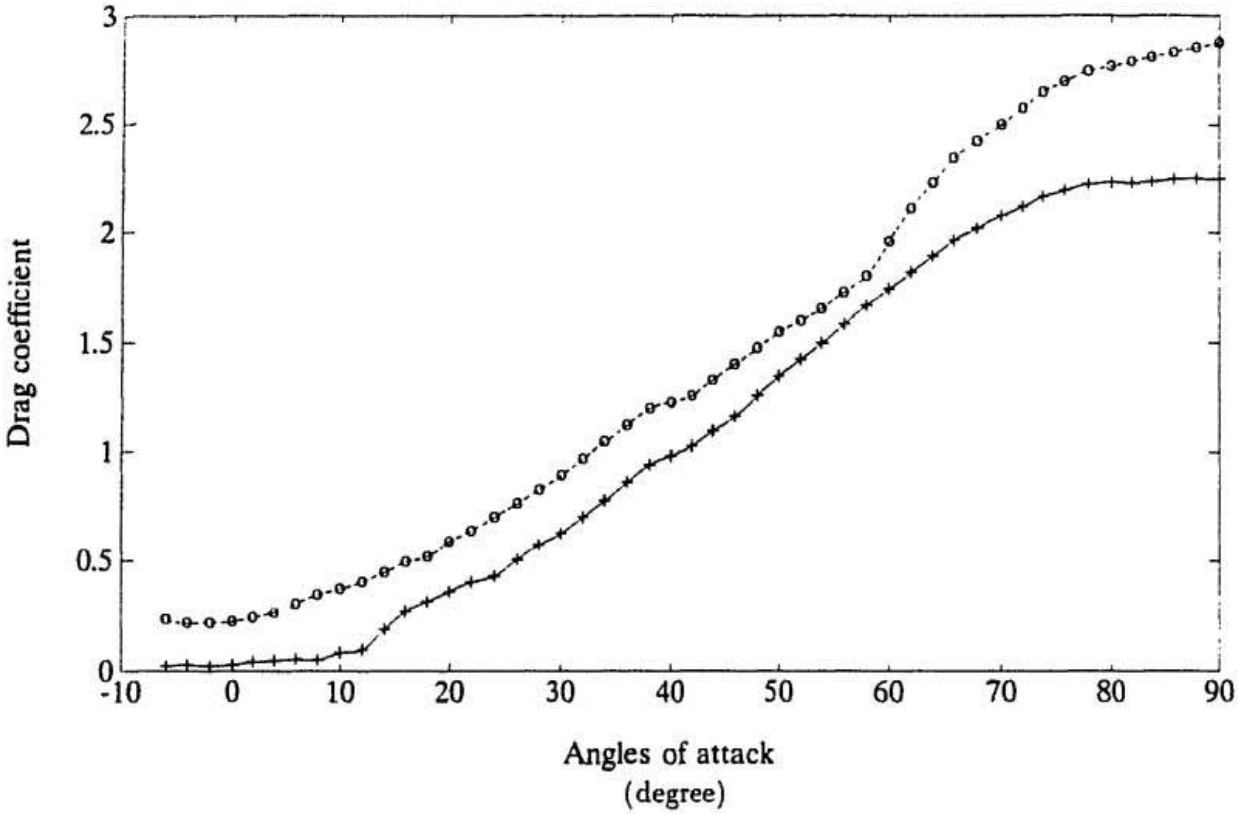

'*': Clean airfoil
'o': Iced airfoil

Figure 4.12: Test results of drag coefficient for NASA LS(1)-0417 clean and glazel iced airfoil.

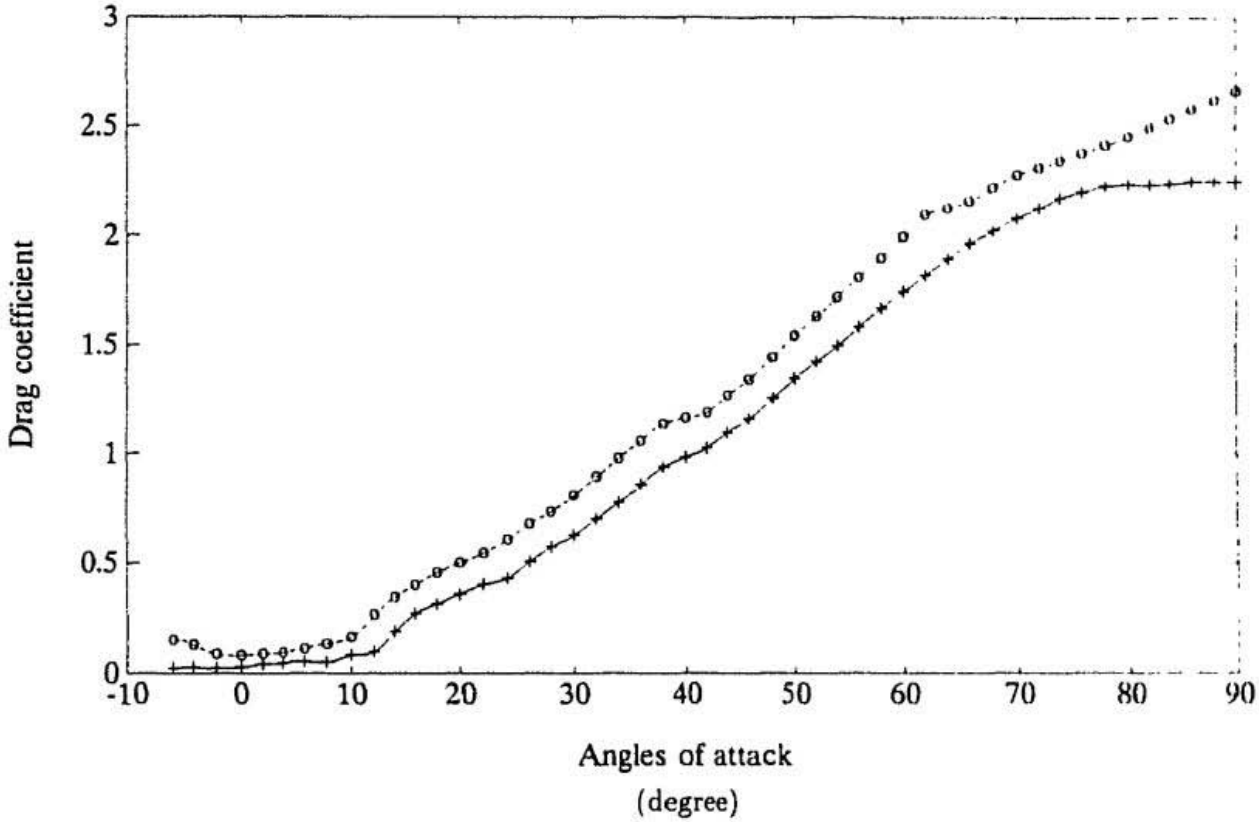

'*': Clean airfoil
'o': Iced airfoil

Figure 4.13: Test results of drag coefficient for NASA LS(1)-0417 clean and glaze2 iced airfoil.

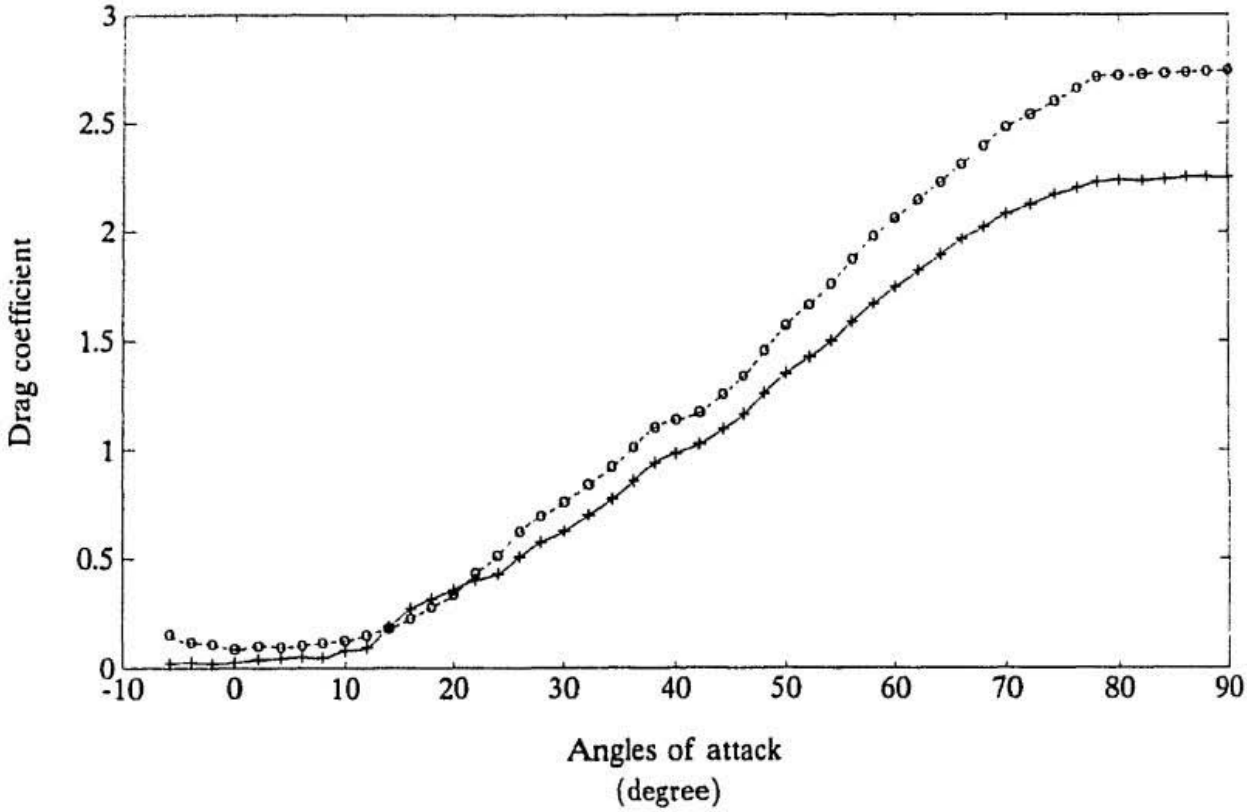

'*': Clean airfoil
'o': Iced airfoil

Figure 4.14: Test results of drag coefficient for NASA LS(1)-0417 clean and rime iced airfoil.

Table 4.1: Coordinates of the NASA LS(1)-0417 airfoil section

x/c	upper (z/c)	lower (z/c)
0.0000	0.00000	0.00000
0.0020	0.01300	-0.00974
0.0050	0.02935	-0.01444
0.0125	0.03069	-0.02051
0.0250	0.01465	-0.02691
0.0500	0.05600	-0.03569
0.0750	0.06561	-0.04209
0.1000	0.07309	-0.04700
0.1250	0.07909	-0.05087
0.1500	0.08413	-0.05426
0.1750	0.08849	-0.05700
0.2000	0.09209	-0.05926
0.2500	0.09778	-0.06265
0.3000	0.10169	-0.06448
0.3500	0.10409	-0.06517
0.4000	0.10500	-0.06483
0.4500	0.10456	-0.06344
0.5000	0.10269	-0.06091
0.5500	0.09917	-0.05683
0.5750	0.09674	-0.05369
0.6000	0.09374	-0.05061
0.6250	0.09013	-0.04678
0.6500	0.08604	-0.04265
0.6750	0.08144	-0.03830
0.7000	0.07639	-0.03383
0.7250	0.07096	-0.02930
0.7500	0.06517	-0.02461
0.7750	0.05913	-0.02030
0.8000	0.05291	-0.01587
0.8250	0.04644	-0.01191
0.8500	0.03983	-0.00852
0.8750	0.03313	-0.00565
0.9000	0.02639	-0.00352
0.9250	0.01965	-0.00248
0.9500	0.01278	-0.00257
0.9750	0.00604	-0.00396
1.0000	-0.00074	-0.00738

Chapter 5

Icing Tests on Horizontal Axis Wind Turbines

Few full-scale wind turbine icing field tests or model tests have been done in the past. The difficulty is that atmospheric icing conditions are usually random and it is always hard to catch the icing event when it happens. Also, icing tunnel tests are rare due to lack of laboratory icing test facilities.

Gustafsson and Meijer [39] estimated the ice build up on the blades or a wind turbine by using a set of different sized cylinders instead of real blades; discrepancies exist between these predictions and results for an actual wind turbine. A series of icing tests on a helicopter rotor are reported by Guffond et al. [31]; the form of the ice deposits on this rotor were similar to our results for a horizontal axis wind turbine rotor. The only work which is considered to be close to the current research is that of Seifort et al.[3]. The test results for a horizontal axis wind turbine under heavy rime icing events show that power loss from the rime icing condition do reduce power output, but is not as severe as that from full scale wind turbine field tests with glaze ice accretion.

5.1 Model Scale Wind Turbine Icing Test

A small scale horizontal axis wind turbine icing test was performed in the cold room of the thermal laboratory in the Faculty of Engineering and Applied Science to document shapes of ice deposits under glaze icing conditions. The cold room has dimensions of length× width× height: 5.6 × 3.85 × 2.4m. The wind turbine model selected had two blades with a fixed pitch of 150mm and was made from wood. The rotor diameter was 302mm. The blade section had one flat surface, the pressure side, and a nearly circular profile on the suction side. The wind turbine model was fixed on an adjustable frame, which was installed at one end of a long table. A fan was used to drive the wind turbine and this kept the wind speed, at the location of the rotor, at about 5m/sec. Before tests, water was cooled down from room temperature to nearly 0°C. Freezing rain was simulated by spraying the water by using a spray gun that was fixed just in front of the fan. This left a 2 meter distance between the spray gun and the wind turbine model, so that the water droplets arriving at the model would be supercooled [40]. The cooled water was pumped through a plastic pipe to the spray nozzle by a micro pump controlled by a variable DC voltage suppiy.

In the test, the room temperature was kept at −5°C, the liquid water content at about 1.6g/m^3 and the diameter of the droplets were around 0.6mm. A sampling tube was used to record the liquid water content by measuring the amount of water collected in a given time. The drop size was measured by using a piece of filter paper. The size of the impinging rain drops was determined by using a spreading factor, S, which was defined as the ratio of the radius of a spread droplet to its initial radius [17]. For a temperature of −5°C and a velocity of 4m/sec , S is equal

to 1.7 [17].

The whole water spray system was dried before being placed in the cold room to avoid blockages due to freezing. The free wind velocity was measured by using a pitot tube and the rotor rotational speed by a light sensitive tachometer (Strobotac meter GR-1538-A).

Two tests were conducted under similar conditions, but with different time durations: 5 and 15 minutes respectively. Before the test, it was observed that the rotor speed varied from 1200 to 1480rpm because the wind generated by the fan was not uniform and caused a change in driving force with time. Soon after the tests, the iced blades were detached and placed on the measuring apparatus shown in figure 5.1. The irregular ice profile was measured by using a clock gauge . The blades were positioned on a block which could slide smoothly along a traverse so that the section data could be recorded in detail; measurements were taken at 0.5mm intervals along the chord. Four blade sections from the tip, $r/R = 1$, to $r/R = 1/5$ were measured by moving the traverse across the span of the blades. Table 5.1 gives the clean blade section offsets measured by using this device. The test results for the ice accretion on the blade section are shown in figure 5.2 and in table 5.2. Figure 5.3 is a photograph of ice deposits on the blades of the wind turbine taken after 15 minutes running time. The results show that the ice deposit shape at the leading edge changes progressively from the blade root to the blade tip. The two protrusions become more pronounced at the blade tips. Much more ice accumulated at the leading edges of the blade tip section, although the radius of the leading edge at the tip is much smaller than elsewhere. These results are somewhat similar to those of Gustafsson and Meijer [39]. Reasons for the differential build up of ice accretion along the blade span are centripetal force and the different relative

wind speed at different blade stations.

5.2 Full Scale Wind Turbine Icing Test

Full scale wind turbine icing tests are necessary to investigate the effects of icing on the performance of wind turbines in field applications and to verify theoretical predictions. As a collaborative project between the Faculty of Engineering and Applied Science at Memorial University of Newfoundland and the Atlantic Wind Test Site (AWTS), a wind turbine icing test was performed at the test site in North Cape, Prince Edward Island. The AWTS is a national centre for wind energy research, development and demonstration in Canada. The machine tested was an Enertech-40 horizontal-axis, down-wind, free-yaw type wind turbine with three blades and three aerodynamic brakes at each blade tip. The wind turbine had a 13.4 m (44 ft) diameter rotor and was fixed on a truss tower about 25 m above the ground. The machine operated at about 60 rpm rotational speed with 40 kW rated power and about a 4.5 m/sec cut in speed.

5.2.1 Test Procedure

Owing to difficulties in catching a natural icing event during a limited three weeks test period, an artificial wind turbine icing test was conducted to simulate atmospheric conditions of glaze ice formation. Figure 5.4 shows the scene of the wind turbine artificial icing test at the AWTS. This test was scheduled to last one hour under clear weather conditions.

Freezing rain was simulated by using a water spray system. A steel frame was fastened on the nacelle in order to fix the spray hose upwind of the wind turbine so that the water droplets sprayed from the nozzles were always upstream of the

rotor. Three nozzles were arranged evenly on the hose from the centre to the edge of the rotor. The distance between the spray nozzles and the rotor was kept to about 4 m to allow the water droplets to have enough time to be supercooled when they reached the blades. The spray system consisted of a high pressure pump which could supply water at a maximum rate of 7 gallon/min under a pressure of 1500 psi; a high pressure hose; three spray nozzles with fine aperture; and a 250 gallon water tank in which the water was kept near to its melting point. A Campbell Scientific data acquisition system was used to monitor the variation of wind velocity, ambient temperature and power output from the Enertech wind turbine at a sampling rate of 1 per second. An ice shape recorder was made to record the ice profile around the blade after the icing test (see figure 5.5). Due to a limit on the number of spray nozzles, the water spray area over the rotor disc covered about one sixth of the whole blade's swept area from the blade tip to the root. This slightly changed the formation of ice accretion on the blade from that which would occur naturally.

The test was done in an ambient temperature range from $-2.7°C$ to $-3°C$, an average wind velocity of about 7m/sec and the water droplet diameter was about 0.5mm. Before the test, the clean wind turbine was run for about 15 minutes to check the data acquisition system and that the wind turbine machine itself was in normal operating conditions. The wind turbine continued to rotate until about 40 minutes after water spray was started when a large piece of ice, with a length almost half that of the blade length, shed off from one blade. The sudden change of mass on this blade caused high acceleration on the rotor and forced the tip brake to release and the machine was shut down for safety. Figure 5.6 shows the ice accumulation on the blades and a large piece of ice shed from one blade.

5.2.2 Test Results

Soon after the test, the ice profile was recorded at one blade section 0.43 m away from the blade tip.

The wind velocity and power output from the wind turbine during the icing event were recorded and are plotted in figure 5.7. The average power curve for the Enertech-44-40 wind turbine with a clean rotor is shown in figure 5.8; this latter was recorded by the Atlantic Wind Test Site.

Power losses were prominent during the icing test. The average power output at the beginning of the test for the clean wind turbine was about 10 kW and this reduced to near zero after 16 minutes of icing. Power output reached about -5 kW just before the end of the test. The negative means that not only does the wind turbine lose the driving torque from the wind, but also power needs to be consumed from the utility grid to keep the machine running. Total loss of power occurred due to the icing. The sudden change in the power output curve in figure 5.7 from about -5 kW to about -23 kW is because of the release of the tip brake.

After the icing test, the ice accretion was almost equally distributed on the three blades, but it was not uniform along each blade span because of the limited number of spray nozzles. Most of the ice accretion built up near to the leading edges; the ice was transparent with blunt shapes. No ice accumulated over most of the suction side of the blades. The ice covered about one third of the pressure side of the blades along the chord length and was rough and soft as shown in figure 5.9.

The icing test showed that freezing rain can cause a blunt glaze ice formation on the leading edge of a wind turbine's blades as shown in the figure 5.9. The ice effect on the aerodynamic performance of the horizontal axis wind turbine was found to

cause a total loss in power absorbed from the wind by this machine in this wind speed.

5.2.3 Comparison with Natural Icing

A full scale wind turbine natural icing test was done by Bose [41].

A horizontal axis Windstream turbine was used. This turbine had a 1.05 m diameter rotor with two blades made from wood and with uniform chord length.

It was installed at St. Phillips, Newfoundland for the period December 1990 to April 1991. Ice accretion shapes were measured during natural freezing rain events. Figure 5.10 shows a measured glaze ice profile at the blade radius fraction $r/R = 0.75$. This result was obtained at 17:30 on 5th March 1991, after a glaze icing event that had been incident since early in the morning; the low lying air temperature was $2°C$.

In comparison with this natural ice formation, the simulated glaze ice profile showed a quantitative variation near to the leading edge because of the different time durations between the artificial and natural icing tests, different geometric size of the blades and different value of liquid water content in the air (this was higher in the natural icing test). Also, there were differences in the ice formation on the pressure side of the blades due to the intermittent nature of the impingement of water droplets on the blades in the simulated icing test that arose because the water was only sprayed out over a sector of the rotor disc area. These conditions also meant that there was a lower temperature on the surface of the ice accretion because of the period during each blade rotation cycle when no water droplets were incident. This led to less motion of the water droplets on the surface of the blade and a rough, soft ice accretion on the pressure side of the blades formed. The test

results show that the power loss from a horizontal-axis wind turbine during freezing rain events can be severe even if the time duration of the icing event is short. The ice formation from an artificial icing test was similar to that from naturally formed icing on a wind turbine blade. If both these tests have the same time duration and similar atmospheric conditions, such as wind velocity, temperature, liquid water content in the air and dimension of the water droplets, then the results from an artificial icing test would be expected to reflect real natural ice accretion on the blades of a wind turbine. Total power loss can result even with a small amount of ice accretion.

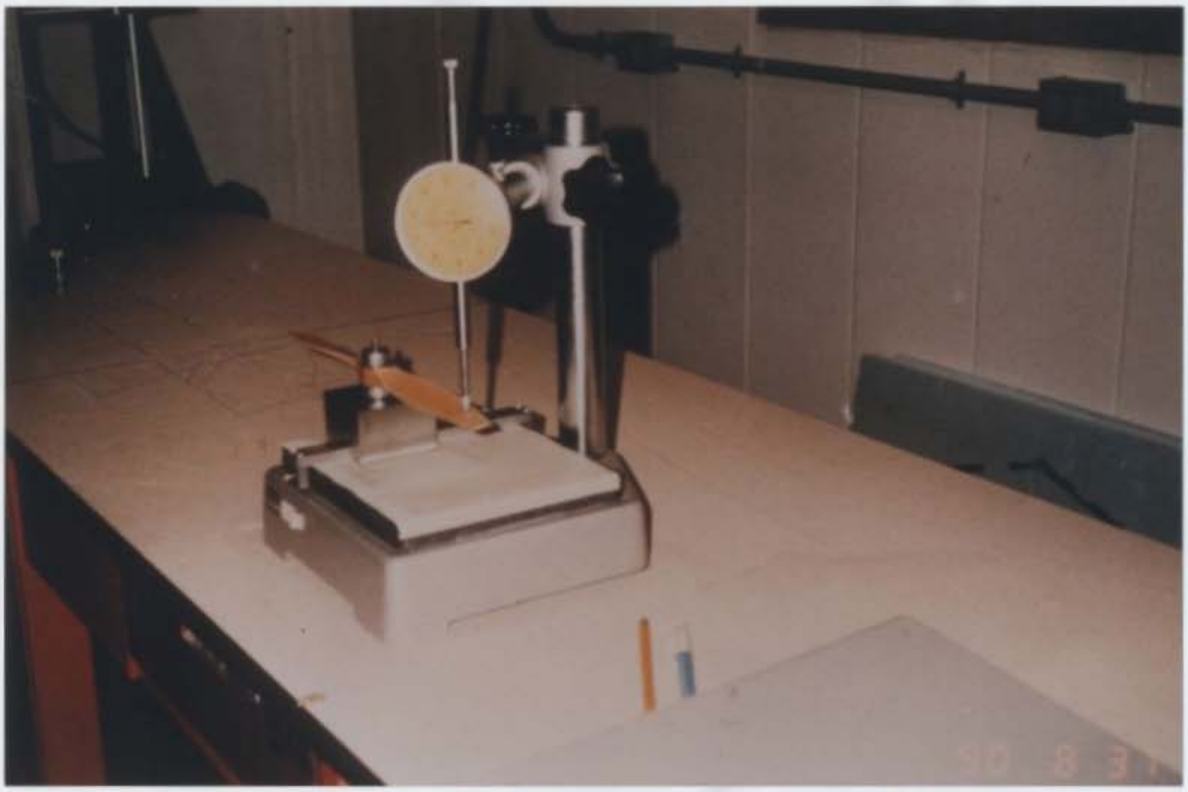

Figure 5.1: Clock gauge table for measurement of ice profile in cold room tests.

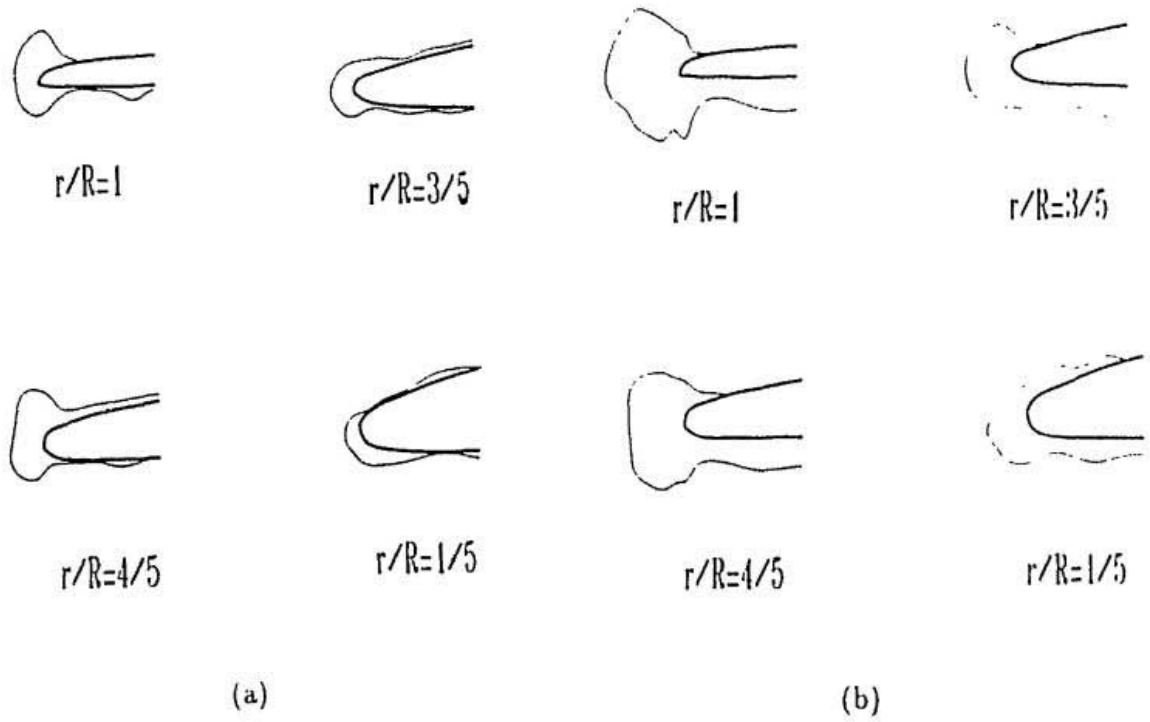

Figure 5.2: Glaze ice profile at various blade sections from cold room tests. (a) 5 minutes time duration, (b) 15 minutes time duration.

(a)

(b)

Figure 5.3: Ice deposits on the blades of the wind turbine model after 15 minutes icing test, (a) Front view, (b) Side view.

Figure 5.4: Scene of icing test in the Atlantic Wind Test Site Inc..

Figure 5.5: Ice shape recorder.

Figure 5.6: A view of ice accretion on the wind turbine's blades and a piece of ice shed from one blade (left blade) after 40 minutes icing test.

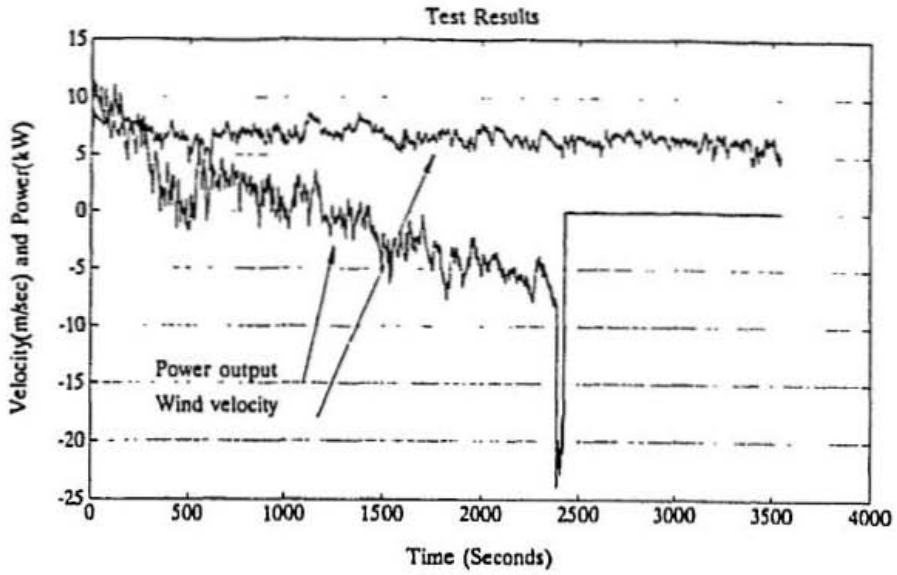

Figure 5.7: Measured curves of wind speed and power output during the icing test.

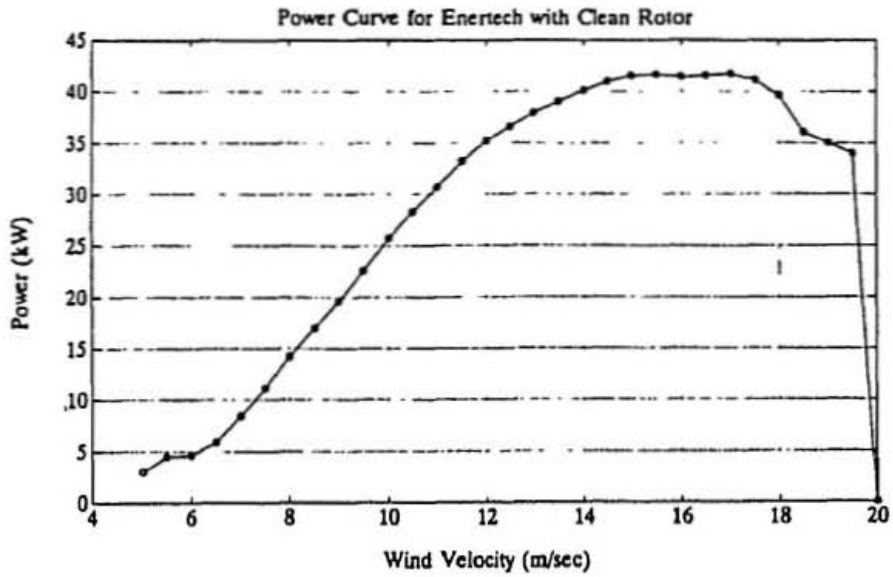

Figure 5.8: Enertech-40 power curve for clean rotor.

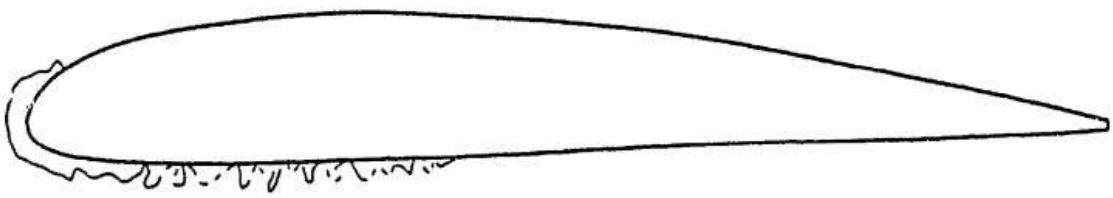

Figure 5.9: Glaze ice profile recorded from the icing test, at 0.43m away from the blade tip after a 40 minute icing test duration.

Figure 5.10: Ice accretion at the radius fraction $r/R = 0.75$ of a Windstream small wind turbine, after a glaze icing event of several hours duration from Bose [41].

Table 5.1: Clean blade section of the wind turbine model used in cold room tests. The X and Z coordinates are given in mm. Section 1: r/R=1, section 2: r/R=4/5, section 3: r/R=3/5, section 4: r/R= 1/5.

Section 1			Section 2		Section 3		Section 4	
X	Z_{lower}	Z_{upper}	Z_{lower}	Z_{upper}	Z_{lower}	Z_{upper}	Z_{lower}	Z_{upper}
0	15.95	16.4	17.11	17.79	18.75	19.14	20.45	20.93
1	15.86	16.83	17.54	19.42	19.34	21.25	21.34	24.18
2	15.72	16.88	17.37	19.51	19.15	21.50	20.95	24.84
4	15.52	16.93	17.00	19.67	18.58	22.51	19.78	24.64
6	15.17	16.68	16.61	19.64	18.09	21.53	18.62	24.08
8	14.98	16.55	16.36	19.75	17.58	21.52	17.47	23.30
10	14.62	15.99	15.89	19.24	17.05	21.28	16.20	21.83
12	14.34	14.93	15.52	18.79	16.53	20.93	15.04	20.18
14			15.18	18.23	15.95	20.32	13.82	17.98
16			14.75	17.35	15.49	19.80	12.65	15.66
18			14.42	16.46	15.00	19.02	11.88	13.51
18.5							11.12	11.15
19			14.18	15.72				
20			13.98	14.04	14.45	17.92		
22					13.95	16.68		
24					13.42	15.08		
25					12.39	13.44		

Table 5.2: Iced blade sections with icing time duration: 5 min, LWC: $1.67 g/m^3$, temperature: $-5°C$ and wind velocity: 4m/s. Section 1: r/R=1, section 2: r/R=4/5, section 3: r/R=3/5, section 4: r/R= 1/5, (unit: mm).

Section 1			Section 2		Section 3		Section 4	
X(mm)	Z_{lower}	Z_{upper}	Z_{lower}	Z_{upper}	Z_{lower}	Z_{upper}	Z_{lower}	Z_{upper}
-2			14.62					
-1.5			14.06					
-1	15.2		13.6	16.52	12.52			
-0.5	15.02	17.52	13.47	17.35	12.08	14.57		11.74
0	14.57	18.75	13.39	17.49	11.92	14.85	10.30	12.16
0.5			14.12	17.08	12.1	15.09	10.12	13.18
1	15.41	17.87	14.31	17.02	12.57	15.24	9.96	13.94
2	16.09		14.48	17.40	12.72	14.44	10.32	15.60
3	16.21		14.69	17.74	12.83	16.18	11.1	
4	16.18		14.65	18.08	13.24	16.64	12.07	
5	15.94		15.00	18.44	13.39	17.14	12.64	
6	16.58		15.39	18.74	13.79	17.62	12.97	
7	16.68		15.39	19.05	13.84	18.09	13.42	
8	16.74		15.57		13.54	18.47	13.95	
9	16.78		15.77		13.70	18.92	14.50	
10	16.75		15.68		13.69	19.28	15.15	
11	17.01		15.87		15.25	19.61	15.08	
12	17.18		16.30		15.32		16.58	
13	17.35		16.35		15.30		17.07	
14			16.54		15.65		17.38	
15			16.70		16.00		18.53	
16			16.78		16.16		19.35	
17			17.15		16.35		19.74	
18			17.18		16.60		19.74	
19			17.22		16.86			
20			17.68		17.53			
21					17.64			
22					17.50			
23					18.20			
24					18.00			
25					18.41			

Chapter 6

Discussion of Current Research

6.1 Formation of Ice Accretion on the Blades

Two typical types of ice accretion, known as rime and glaze ice, may exist on wind turbine blades as described in chapter 2. Each of them forms a unique ice profile around the leading edge and pressure side of the blade under certain atmospheric conditions. Rime ice, shown in figure 1.2, usually happens when ambient temperature and liquid water in the air is low and glaze ice, shown in figure 1.1 happens when the temperature and liquid water content in the air is relatively high.

Analysis shows [1,2] that shapes of ice accretion are strongly governed by the ambient temperature, quantity of supercooling of water droplets, liquid water content in the air and relative wind velocity. Higher ambient temperature can slow down the rate of heat convection and conduction between the accretion surface and the air as illustrated in section 2.4, which results in decrease of release rate of latent heat from the water droplets during nucleation. Decrease in amount of supercooling of the water droplets can reduce the rate of nucleation as expressed by equation 2.2. Droplet size may effect the rate of impingement of the droplets on the blade because of their different momentum; the bigger the droplet, the higher

possibility of impingement on the blade. A larger amount of liquid water content in the air requires more time to release latent heat and to exchange heat flux to fulfil the icing process when the water droplets impinge on the blades. Due to the above conditions, the temperature of the ice accretion surface may be near 0° before the next water droplet hits the same area and, therefore, there may be a portion of the unfrozen water droplets on the accretion surface providing conditions for run back and hence blunt or horn-like ice accretions form. These conditions are usually associated with glaze ice accretion that has low porosity and is transparent.

The resultant wind velocity is also critical in ice formation. The higher the relative wind velocity, the higher the pressure gradient near the stagnation point at the leading edge of the blade. This implies that the unfrozen water droplets can run back faster away from the leading edge near the stagnation point, and this is more likely to build blunt or horn-like ice accretions. The results from the cold room test shows that the two protrusions become more pronounced near the blade tips, as illustrated in figure 5.2; a higher relative wind velocity is located at the blade tips.

Rime ice forms when the temperature and liquid water content in the air are lower. These give the conditions that unfrozen water droplets in the air are highly supercooled and the water droplets can freeze immediately on impingement. Due to very little freezing time required, water droplets freeze when and where they arrive on the blade surface and hence, rime ice accretions are more streamlined (see figure 1.2).

6.2 Performance Degradation of Iced Airfoil

Wind tunnel tests for a NASA LS(1)-0417 airfoil tests showed that sharp decrease of lift coefficient occurred below and in the stall regions for the glaze iced forms tested and sharp increase of drag coefficients occurred for both glaze and rime iced forms as shown in figures 4.9 to 4.14. Significant performance degradations were encountered for glaze 1 and glaze 2 icing. Lift coefficient was almost destroyed in glaze 1 icing over the angles of attack from 0° to 10°. The maximum drop of lift coefficient for glaze 2 was 38% at 4° angle of attack. Increase of drag coefficients occurred over the full range of angles of attack (−6° to 90°) in both glaze and rime icing. The average increase in drag coefficients over angles of attack from −6° to 12° was about 500% for glaze 1 icing, 180% for glaze 2 icing and 150% for rime icing. The lift coefficients for the airfoil with both glaze ice forms were higher than that of the clean airfoil after the stall region.

These results can be explained by flow theory. Basically, the lift and drag coefficients are two components of the resultant aerodynamic force exerted on an airfoil. These two forces result from the pressure distribution on the surface of the airfoil and are governed by the velocity distribution around the airfoil. The velocity profile in the boundary layer and the rate of increase of boundary layer thickness around an airfoil depend on the pressure gradient in the direction of flow motion. If the pressure increases in the direction of the main flow, the boundary layer thickness increases rapidly and the velocity profile in the boundary layer is distorted. If this pressure gradient is large enough, then separation will occur followed by a region of reversed flow or reversed velocity profile. This is usually associated with increase of pressure drag by changing the pressure distribution around the blade section.

In the case of glaze ice formation, there are abrupt changes of the profile near the leading edge and the airfoil is no longer streamlined, especially at large angles of attack. As the flow approaches the ice horn, the flow separates from the ice surface at the tip of the horn, and forms a separation bubble due to the adverse pressure gradient in the flow direction. If the angle of attack is low, the separated flow may reattach to the airfoil surface further back on the profile before it is shed from the airfoil, and the aerodynamic properties are not changed significantly. If the glaze ice accretion is heavy, severe flow separation can occur even at low angles of attack. When separated flow can not reattach to the airfoil, the boundary layer remains separated. This leads to a loss of circulation and results in a sharp decrease in lift. Also, the separation and distorted boundary layer, together with the friction of the rough ice surface, result in significant increased drag. As the rime ice profile tested did not severely distort the streamlined shape of the airfoil, its effect on the aerodynamic performance of the section was less than that of the glaze ice accretions tested. The explanation of increase in lift coefficients after the stall region for the iced airfoil is that the lift coefficients for different shaped airfoils are almost the same at higher angles of attack [42], which implies that the shape of airfoil is no longer critical; the chord length of the airfoil was increased by the ice accretion on the leading edge, which resulted in an increase in total lift force exerted on the airfoil.

6.3 Evaluation of Power Losses by Icing

Calculations were made to estimate power losses from a 2.5m diameter horizontal axis wind turbine and a Carter WEC-23 horizontal axis wind turbine under the rime and glaze icing conditions that were simulated in chapter 4. Rime ice accretion had

a much less severe effect on the performance degradation of these wind turbines than glaze ice accretion, even though the rime ice accretion was heavy; this was also shown by Seifert and Scholtz [3]. The glaze ice forms reduced the power output from the wind turbine in a significant way. The force diagram in figure 3.4 shows that the tangential component of lift force acts in the direction of a wind turbine's driving torque and that the drag force acts as a resistance torque. Glaze ice results in a sharp increase in pressure drag and decrease in lift and therefore, decrease in the torque coefficients and power ratio for the wind turbines due to loss of driving torque and increase of resistance torque. Power reduction from the wind turbine in these conditions can be very severe.

Figures 3.6 to 3.11 shows the power ratio for the 2.5 m diameter and the Carter-23 wind turbines over tip speed ratios from 0.5 to 12.

Rime icing reduced power output from the 2.5 m diameter wind turbine by 49% and from the Carter-23 wind turbine by 30%. Both glaze icing events destroyed the aerodynamic performance of the wind turbines completely in this range of tip speed ratio. As both the glaze icing events simulated lasted only about six minutes, this implies that atmospheric icing conditions may destroy the performance of a wind turbine significantly within a short time period.

The theoretical predictions for power reduction from wind turbines by glaze icing on the blade were verified by a wind turbine field icing test. Figure 5.7 shows that power losses from an Enertech-40-44 wind turbine were prominent during the icing test. The average power output at the beginning of the test for the clean wind turbine was about 10 kW and this reduced to near zero after 16 minutes of icing, almost a 100% power loss at this icing event and at this wind speed.

Finally, an example is given to show annual power losses from a wind turbine

due to freezing precipitation. The assumption is made that this Carter-23 wind turbine is installed near to North Cape on Prince Edward Island, Canada, and the average wind speed located at 30 m above the ground in the winter is 8.4 m/sec (data was from the Atlantic Wind Test Site). The mean residence time of freezing precipitation occurring near Summerside, Prince Edward Island is about 121 hr/yr [8]. The power output from the Carter-23 wind turbine at this wind speed is about 110 kW. Therefore, the annual power losses from this machine due to glaze icing is about 13 MWHr!

Chapter 7

Conclusions from the Research

This research has provided quantitative information on the effects of icing on wind turbine generators. This is important for the use of wind energy in high icing zones of Canada, often the same areas where the wind energy resource is high.

This thesis describes both experimental and theoretical analysis of icing effects on horizontal axis wind turbines. Specifically, a wind turbine model was tested in a cold room under icing conditions, wind tunnel tests for an airfoil with different simulated ice accretions were carried out in a low speed wind tunnel and an icing field test was done for an Enertech-40-44 horizontal axis wind turbine at the Atlantic Wind Test Site. Numerical evaluations were made for the performance degradation of a 2.5 m diameter horizontal axis wind turbine and a Carter WEC-23 wind turbine as a result of icing on their blades.

Simulation of freezing rain events and glaze icing was done on a small model wind turbine rotor in a cold room. The results showed that accreted ice shapes changed progressively from the blade root to tip. Much more ice deposited at the leading edge at the blade tip than at the root, where resultant relative wind speed was higher and local radius in the leading edge of the blades was smaller. The accreted ice at the leading edge of the blades was more prominent and had blunt

or horn-like shapes in the higher speed region near to the blade tips. The glaze ice accretion with blunt or horn-like shapes occurred in atmospheric conditions of ambient temperature close to the freezing point; liquid water content in the air above 1.6g/m^3; larger water droplets size and relatively high wind speed.

Wind tunnel tests were done to obtain coefficients of lift and drag for a NASA LS(1)-0417 wing section with simulated ice accretion at the leading edge. Results showed that performance degradation for the airfoil by icing is severe. Significant performance degradation was encountered for two types of glaze accretion denoted as glaze1 and glaze2 icing. Lift coefficient was almost destroyed for glaze 1 icing in the range of the angles of attack from 0° to 10°. The maximum drop of lift coefficient for glaze 2 was 38% at an angle of 4°. Increase of drag coefficients occurred during both glaze and rime icing over a full range of angles of attack from −6° to 90°. The average of increase in drag coefficients over angles of attack from −6° to 12° was about 500% for glaze 1 icing, 180% for glaze 2 icing and 150% for rime icing. These performance changes are the main reason for power reduction from wind turbines due to icing.

Theoretical performance predictions were made for a 2.5 m diameter and a Carter-23 horizontal axis wind turbines with iced blades by using lifting-line theory. These were two bladed machines. The power output from these wind turbines were reduced significantly by glaze icing. Calculation results showed that rime icing reduced power output from the 2.5 m diameter wind turbine by 49% and from a Carter-23 wind turbine by 30%, but glaze icing events destroyed the aerodynamic performance of the wind turbines completely in the range of tip speed ratio assumed from 0.5 to 12. As both glaze icing events simulated were formed in an icing wind tunnel after only about six minutes, this implied that atmospheric icing conditions

will destroy the performance of a wind turbine seriously in a very short time period.

A full scale wind turbine field icing test was done with a time duration of 40 minutes. The results show that the average power output at the beginning of the test for the clean wind turbine was about 10 kW and this reduced to near zero after 16 minutes of icing, that is almost a 100% power reduction.

Power loss from a horizontal-axis wind turbine during freezing rain events can be very severe even if the time duration of the icing event is short. However, it is likely that in conditions of heavy icing, the machines would be shut down automatically when significant rotor vibration occurs; this results in further power reduction.

Due to high incidence of freezing precipitation in most Atlantic and Coastal regions of Canada where the wind energy potential is high, steps should be taken to prevent wind turbines from icing, especially from icing on the wind turbine blades. Design of wind turbine blades which are insensitive to small scale ice accretions would alleviate power losses. In heavy icing, however, deicing techniques for the wind turbine blades might be used. The wind turbine deicing device should be cost effective to keep down the cost of energy production from wind generators and hence increase the competitiveness of wind energy technology in these cold regions.

References

1 Mortimer, A.R., ' A review of the icing problem for aerogenerators', Wind Engineering, 1980, Vol.4, No.4, pp. 183-191.

2 Makkonen, L. and Autti, M., ' The effects of icing on wind turbines', Proceedings of European Wind Energy Conference, October 1991, Amsterdam, Netherland, 5 pages.

3 Seifort, H. and Schloz, C., ' Additional loads caused by ice on rotor blades during operation', European Community Wind Energy Conference, Madrid, H.S. Stephens and Associates, 1990, pp. 203-207.

4 Rong, J.Q. and Bose, N., 'Power reduction from ice accretion on a horizontal axis wind turbine', Proceedings of the British Wind Energy Conference, March, 1990, Norwich, Britain, 6 pages.

5 Rong, J.Q. and Bose, N., 'Studies of glaze icing effects on a horizontal axis wind turbine', Proceedings of the Canadian Wind Energy Conference, October,1990, Banff, Alberta, Canada, pp. 209-223.

6 Rong, J.Q., Bose, N., Brothers, C. and Lodge, M, 'Icing test on a horizontal axis wind turbine', Journal of Wind Engineering, Vol.15, No.2, 1991, pp. 109-113.

7 Rong, J.Q., Bose, N. and Brothers, C., 'Wind tunnel tests on a wind turbine blade section with simulated glaze and rime icing', Proceedings of the Canadian Wind Energy Conference, November, 1991, Montreal, Canada (in press).

8 Kolomeychuk, R. and Silis, A. 'Preliminary investigation of the potential effects of icing on wind energy system performance', paper of the Renewable

Energy Branch, 1987, Energy, Mines and Resources, Canada, DSS file No. 54SZ.23216-6-6119.

9 Goldstein, S., 'On the Vortex Theory of Screw Propellers', Proceedings of the Royal Society, London 1929, Vol.A 123, pp.440-465.

10 Lerbs, H.W., 'Moderately loaded propellers with a finite number of Blades and an arbitrary distribution of circulation', Transactions of the Society of Naval Architect and Marine Engineers, New York, 1952, Vol. 60, pp. 73-123.

11 O'Brien, T.P., 'The design of marine screw propellers', Hutchinson, Scientific and Technical, 1962.

12 Small, G.H., 'Performance calculations for a wind turbine using liftline theory', University of Glasgow Marine Technology Centre, Scotland, 1985, Report No. NAOE-85-47.

13 Small, G.H. and Bose, N., 'Further additions to the liftline theory ', University of Glasgow Marine Technology Center, Scotland, 1986, Report No. NAOE-86-48.

14 Bose, N., 'Wind turbine assisted propulsion of marine vehicles', University of Glasgow Marine Technology Center, Scotland, 1986, Report No. NAOE-86-39.

15 Wilder, R.W., ' A theoretical and experimental means to predict ice accretion shapes for evaluating aircraft handling and performance characteristics', The Boeing Company, Seattle, Washington, Aircraft Icing, 1978, 12 pages.

16 Bragg, M.B., ' The effect of structural ice on aircraft component aerodynamics', Fourth International Conference on Atmospheric Icing of Structures, Paris, 1988, pp. 134-138.

17 Macklin, W.C. and Payne, G.S., 'Spreading of accreted droplets', Journal of Royal Meteorological Society, Oct. 1969, Vol.95, pp. 724-730.

18 Hunter, M., 'Report for Bell island wind demonstration project', Newfoundland Light and Power Company, 1988.

19 Michel, B., ' Ice mechanics', Les Presses de L'Universite Laval, Quebec, Canada, 1978.

20 Lozowski, E.P., 'The icing of an unheated, nonrotating cylinder, Part one: A simulation model', Journal of Climate and Applied Meteorology, May 1982, pp. 2053-2062.

21 Lozowski, E.P., 'The atmospheric icing: a review', Fourth International Conference on Atmospheric Icing of Structures, Paris, 1988, 5 pages.

22 Seban, R.A., 'The influence of free stream turbulence on the local heat transfer from cylinders', Journal of Heat Transfer, 1982, 7 pages.

23 Glauert, H., ' An aerodynamic theory of the airscrew', Aeronautical Research Council, Reports and Memorandum, AE. 43 No. 786, 1922.

24 Joukowski, N.E., Soc. Math. Moscow, 1912, reprinted in 'Theorie tourbillonnaire de l'helice propulsive', Paris, 1929.

25 Betz, A., 'Screw propellers with minimum energy loss', Transaction of Association of Science of Gottingen, Mathematics-Physics Class, 1919, pp. 193-217,

Translated by T. Hofmann, Edited by N. Bose, Memorial University of Newfoundland, St. John's, Newfoundland, Report No. OERC90-HYD-LR-02, 1990.

26 Eckhardt, M.K. and Morgan, W.B., 'A propeller design method', Transaction of the Society of Naval Architectures and Marine Engineers, New York, 1955, Vol.63, pp. 325-374.

27 Tachmindji, A. and Milam, A., ' The calculation of Goldstein factors for three, four, five and six bladed propellers', Navy Department, The David W. Taylor Model Basin, Washington 7, D.C., Report No. 1034, 1956.

28 Bragg, M.B., ' Wind tunnel evaluation of airfoil performance using simulated ice shapes', Prepared for National Aeronautics and Space Administration, Lewis Research Center, November 1982, 31 pages.

29 Bragg. M.B., ' Predicting airfoil performance with rime and glaze ice accretion', AIAA Paper, January 1984, No. 84-0106.

30 Bragg, M.B. and Coirier, W.J., 'Detailed measurements of the flow field in the vicinity of an airfoil with glaze ice', AIAA Paper, January 1985, No. 85-0409.

31 Guffond, D., Cassaing, J., Henry, R. and Bossy, M.,'Overview of Icing Research at ONERA', Fourth International Conference on Atmospheric Icing of Structures, Paris, 5-7 Sep.1988, pp. 186-191.

32 Cebeci, T., ' The calculation of flow over iced airfoils', AIAA Paper, 1988, No. 88-0112.

33 Potapczuk, M.G., 'Numerical analysis of a NACA0012 airfoil with leading edge ice accretions', AIAA Paper, 1987, No. 87-0101.

34 Oleskiw, M.M. and Lozowski, E.P., 'Helicopter rotor blade icing, a numerical simulation', International Conference on Cloud Physics, 1980, Clermont-Ferrand, France, pp. 281-284.

35 Potapczuk, M.G. and Berkowitz, B.M., 'An experimental investigation of multi element airfoil ice accretion and resulting performance', NASA N89-15084, 1989.

36 Lock, C.N.H., 'The interference of a wind tunnel on a symmetrical body', Aeronautical Research Council, Reports and Memorandum, 1929.

37 Pankhurst, R.C. and Holder, D.W., 'Wind tunnel technique', Sir Isaac Pitman and Sons, Ltd, London, 1965.

38 Glauert, H., ' Wind tunnel interference on wings, bodies and airsrews', Aeronautical Research Council, Reports and Memorandum, 1933.

39 Gustafsson A. and Meijer S., 'Preparatory icing studies for Swedish prototype WECS', Fourth International Symposium on Wind Energy Systems, Stockholm, Sweden, Sept. 21-24, 1982, pp. 377-388.

40 Stallabrass, J.R., 'Aspects of Freezing Rain Simulation and Testing', Proceedings of First International Workshop, Atmospheric Icing of Structures, Special Report 83-17, 1983, pp. 67-73.

41 Bose, N., 'Sensitivity of wind generator output to icing conditions, report of work done from April 1990 to March 1991', Faculty of Engineering and

Applied Science, Memorial University of Newfoundland, St. John's, Nfld, Canada, March 12, 1991, EAST Report No. 91-002.

42 Hoerner, S.F., ' Fluid dynamic lift', Fluid dynamic drag, Albuquerque: Hoerner Fluid Dynamics, 1965.

APPENDIX

Results of Wind Tunnel Calibration:

	A1	A2	A3	A4	A5	A6		B1	B2	B3	B4	B5	B6	
U	10	12	13	14	14	14		11	12	14	14	14	14	
Tb	10	6	5	1.7	0.9	0.7		10	7	5	1.6	1	0.8	
	C1	C2	C3	C4	C5	C6		D1	D2	D3	D4	D5	D6	
U	10	11	12	13	14	14		9	10	12	13	13	13	
Tb	12	10	7	4	1	0.8		10	9	6	2.5	1	0.9	
	E1	E2	E3	E4	E5	E6	E7	F1	F2	F3	F4	F5	F6	F7
U	8	9	10	11	13	13	13	8	10	12	13	13	13	13
Tb	16	16	15	12	7	4	3	17	13	8	5	3	1.6	1
	G1	G2	G3	G4	G5	G6	G7	H1	H2	H3	H4	H5	H6	H7
U	9	10	12	13	13	13	13	9	11	12	13	13	14	14
Tb	15	11	9	5	4	4	4	15	12	9	5	3	2	1

Note: 1. U is a local wind speed in the wind tunnel in m/sec; Tb is a local turbulence in %
2. See figure 4.2 to locate each point in the tunnel cross section
3. At centre point of the tunnel cross section 'o', U=14 m/sec and Tb=0.7%.